DIFFUSE SOURCE TRANSMISSIBILITY UPSCALING

A Thesis

by

KRISHNA CHAITANYA NUNNA

Submitted to the Office of Graduate and Professional Studies of
Texas A&M University
in partial fulfillment of the requirements for the degree of

MASTER OF SCIENCE

Chair of Committee,	Michael J. King
Committee Members,	Akhil Datta-Gupta
	Yalchin Efendiev
Head of Department,	Dan Hill

December 2014

Major Subject: Petroleum Engineering

ABSTRACT

Static high resolution three dimensional geological models are routinely constructed to provide an integrated description of a reservoir which includes seismic, well log and core data, and which characterize the reservoir heterogeneity at multiple scales. These models also represent the structure and stratigraphy of the reservoir within the design of the modeling grid, which may include faults, fault blocks, pinch-outs, layering and cross bedding. Numerical simulation of these high resolution static models remains a challenge even with the rapid growth of computational resources since both geological and flow simulation models have increased in size. 50 million cell geologic models are routine, while simulation models are typically one or two orders of magnitude coarser. Also, multiple simulations should be performed to optimize among various recovery or well placement scenarios for subsurface uncertainty assessment which is not possible to carry out on fine scale models. Hence, upscaling of the geologic models for flow simulation remains part of the subsurface workflows.

The industry also faces new reservoir engineering challenges. Unconventional reservoirs (tight gas / shale oil / shale gas) have low permeabilities ranging from micro to nano Darcy. The time for pressure transients are no longer measured in hours or days, but instead are measured in decades or longer for unconventional systems. The separation between transient testing and steady state reservoir management is no longer applicable.

Historically, our upscaling algorithms have relied upon steady state concepts of flow, which are no longer applicable to unconventional reservoirs.

In the current study, a novel diffuse source transmissibility upscaling approach is described. It applies pressure transient concepts to the calculation of the effective transmissibility between coarse cell pairs. Unlike the usual steady state upscaling algorithms, it is a completely local calculation and is not dependent upon knowledge of, or assumptions about, global reservoir flow patterns. The concept of diffusive time of flight is utilized to calculate the drainage volume at the inter-cell face and remove the fine cells disconnected from the drainage volume.

The approach is validated at field scale using an onshore US tight gas reservoir model and is shown to reduce simulation run times by up to two orders of magnitude without significance loss of accuracy in performance prediction.

DEDICATION

To my parents and friends

for their endless support, love and encouragement

ACKNOWLEDGEMENTS

I would like to thank my committee chair, Dr. Mike King, who has been a tremendous support and guide. Sincere thanks to my other committee members, Dr. Akhil Datta-Gupta, and Dr. Yalchin Efendiev, for their guidance during the course of this research.

A special thanks to all the members of the Model Calibration and Efficient Reservoir Imaging (MCERI) research group for sharing their knowledge and lending me their support. Every person that I met during the course of my masters has had an influence on my work. I wish to be able to apply all the positive things I tried to learn from everyone during this time.

In the end, this journey would not feel the same without the support of my loving family and friends. Their words of encouragement were always my best guides even in the moments of darkness.

NOMENCLATURE

c_t	Total compressibility; psi^{-1};
h	Formation thickness; ft;
k	Permeability; md;
$\vec{\vec{k}}$	Permeability tensor; md;
q	Darcy flux; RB/day;
r	Radius of investigation; ft;
t	Time; hours;
p	Pressure; psi;
A	Cross sectional area; ft^2;
L	Length; ft;
V_p	Drainage volume; ft^3;

Subscripts

eff	Effective
h	Horizontal
i	Index
w	Well

Greek variables and operators

α	Hydraulic diffusivity

τ	Diffusive time of flight
μ	Fluid viscosity
ϕ	Porosity
∇	Gradient

Abbreviations

BRV	Bulk Rock Volume
PSS	Pseudo Steady State
PV	Pore volume
RB	Reservoir Barrel
SS	Steady State

TABLE OF CONTENTS

Page

LIST OF FIGURES

Page

Page

LIST OF TABLES

Page

CHAPTER I

INTRODUCTION

Reservoir simulation is an important component in modern reservoir management as it can provide forecasts for hydrocarbon recovery and aids as a tool for reservoir performance optimization. Reservoir models can be classified into proxy models, mass balance models and detailed 3D reservoir models (King 2011).

Proxy models: Proxy models require minimal time in building and are easy to calibrate against history. They can provide short term predictions like decline curve prediction forecasts or static model based infill ranking. Although, they are fast to build, the models are not well equipped to represent reservoir energy and the progression of fluid fronts.

Mass balance models: Mass balance models are rapid to build and update since they are based only on volumes and transmissibilities. They can represent and accurately predict reservoir energy (reservoir + wells), but the models are not well equipped to represent and predict the fluid fronts or reservoir sweep.

3D detailed reservoir models: Detailed 3D reservoir models can represent and predict the reservoir energy (reservoir + wells) as well as represent and predict the fluid fronts and sweep (water & gas), but they are slow to build & update because of the amount of detail involved in building them.

The workflow for detailed 3D reservoir modeling and simulation (**Figure 1)** starts with building the high resolution static geologic models transitioning into coarse dynamic simulation models. Static models typically contain cells in the order of 10 to 100 million grid cells, providing highly detailed reservoir descriptions. Simulation models are typically one or two orders of magnitude coarser. A geo-modeler builds the geologic model integrating both the well log data and seismic data using geo-statistical techniques. Going from the well log scale to the scale of the blocked wells for the geologic model is a 1D upscaling calculation.

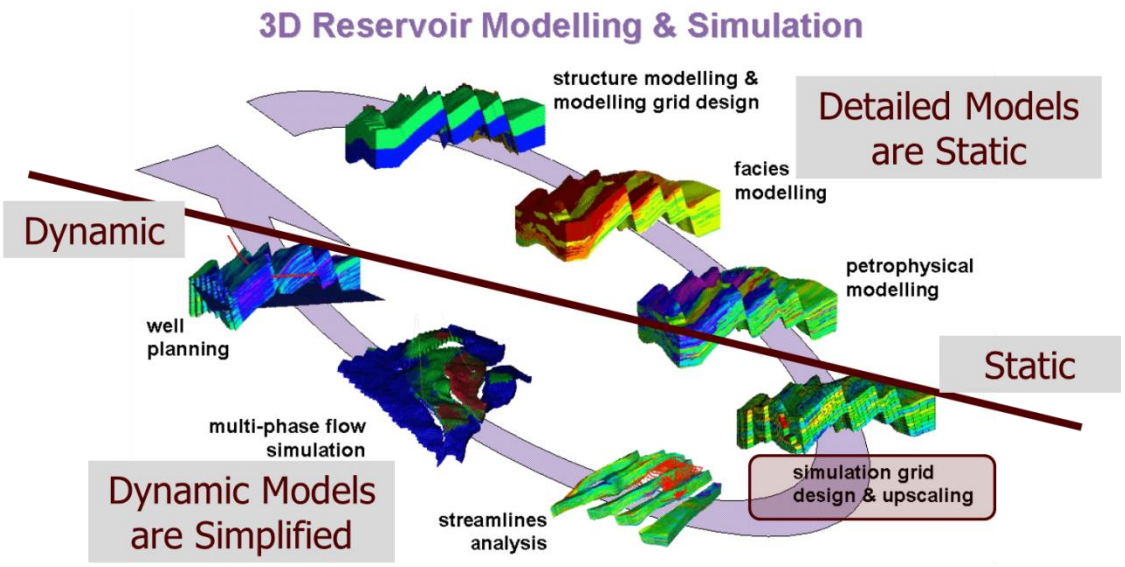

Figure 1: Upscaling in the overall 3D modeling workflow (RMS 2012)

Upscaling is the process of getting the best averaged properties on the coarse grid. Simulation grid design, upgridding, and upscaling are performed at the transition between static and dynamic models. Reservoir characterization is performed on the static geologic models and reservoir simulation is performed on the coarse models which are obtained from upscaling the static models. Numerical simulations using large geological models is still too expensive, even with the rapid advent of computational resources, because, in practice, multiple simulations should be performed in order to optimize among various recovery or well placement scenarios. With a growth in computational resources, the geologic models have also increased in size. Hence, upscaling remains an important component of the reservoir modeling workflow. When done well, upscaling will preserve the most important flow characteristics of a geologic model.

1.1 Literature review

In this section, we review the existing upscaling methods. Upscaling techniques can be broadly classified into traditional upscaling methods and multi scale upscaling methods. In the traditional upscaling techniques, the scales in which the data is represented are changed to a single scale by some kind of averaging procedure and then the problem is solved on the coarse grid. Traditional upscaling methods are further classified into analytical methods and flow based upscaling methods.

1.1.1 Single phase analytical upscaling methods

Single phase analytical upscaling methods are computationally fast and are representative of ideal cases. Renard and de Marsily (1997) summarized the single phase analytical upscaling of the effective permeability.

- **1D Arithmetic average:** It gives the simple arithmetic average of all the permeabilities. **Figure 2** illustrates the conceptual picture where the entire reservoir is re-stacked and placed adjacent to a well so that all of the rock feels the same pressure gradient. The average permeability is given by **Eq. 1.1.** The expression would be exact for the horizontal permeability of uniform layers arranged in parallel.

  $$\bar{k} = \frac{\sum_{i=1}^{N} k_i h_i}{\sum_{i=1}^{N} h_i} \quad (1.1)$$

  where,

  $\bar{k}$, average permeability (md);

  k, permeability (md);

  h, thickness (ft);

- **1D Harmonic average:** Yields an exact answer if the entire reservoir is stacked like a long core so that flow must pass through each and every piece of rock. It gives a good estimate for vertical permeability in the reservoir as shown in **Figure 3**. The effective permeability is given by a thickness weighted harmonic average of the individual permeabilities as shown in **Eq. 1.2.**

$$\overline{k_z} = \frac{\sum_{i=1}^{N} h_i}{\sum_{i=1}^{N} \frac{h_i}{k_i}} \dots\dots\dots\dots\dots\dots\dots\dots\dots\dots\dots\dots\dots\dots\dots\dots (1.2)$$

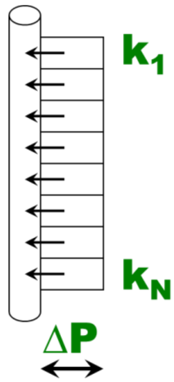

Figure 2: 1D Arithmetic average (King 2011)

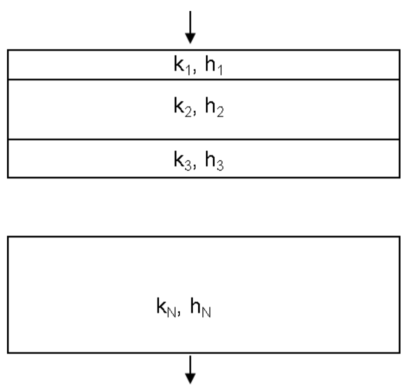

Figure 3: Harmonic average (King 2011)

- **1D Geometric average:** Exact for randomly distributed (uncorrelated) permeabilities in 2D with small variance. The expression for the average permeability is given by **Eq. 1.3.**

$$\log(\bar{k}) = \frac{\sum_{i=1}^{N} BRV_i \log(k_i)}{\sum_{i=1}^{N} BRV_i} \dots\dots\dots\dots\dots\dots\dots\dots\dots\dots\dots\dots\dots\dots (1.3)$$

where,

BRV, Bulk rock volume of the cell (ft^3);

- **1D Power law average:** Generalized averaging technique with the expression for average permeability shown in **Eq. 1.4.**

$$\bar{k} = \left(\frac{1}{N}\sum_{i=1}^{N} k_i^p\right)^{\frac{1}{p}} \quad \ldots\ldots (1.4)$$

The range of p varies from -1 to 1.

  - $p = -1$ (harmonic average)
  - $p = 0$ (geometric average)
  - $p = 1$ (arithmetic average)

In practice, a fine scale simulation is used to calibrate the power exponent.

- **2D/3D Harmonic-Arithmetic average: Figure 4** shows the 2D conceptual picture of the averaging technique where the cross flow is turned off between the layers yielding an arithmetic sum of many core floods (harmonic average) (Warren and Price 1961). It provides a rigorous lower bound estimate of the average permeability.

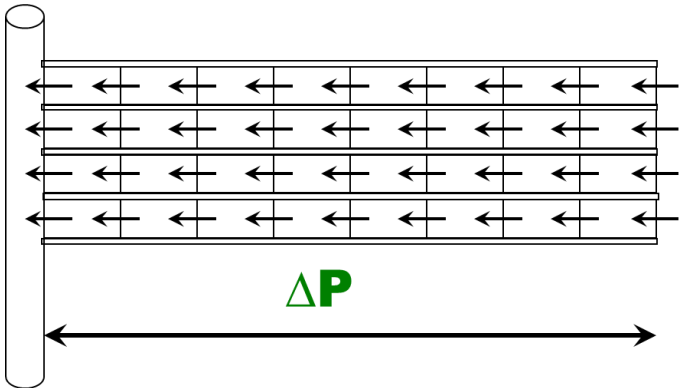

Figure 4: Harmonic-Arithmetic average (King 2011)

- **2D/3D Arithmetic-Harmonic average:** Generates mixing of fluid at each column of the model (arithmetic average), and a single average core flood if there is a perfect transverse pressure equilibrium (Warren and Price 1961). It provides a rigorous upper bound estimate of the average permeability (**Figure 5**).

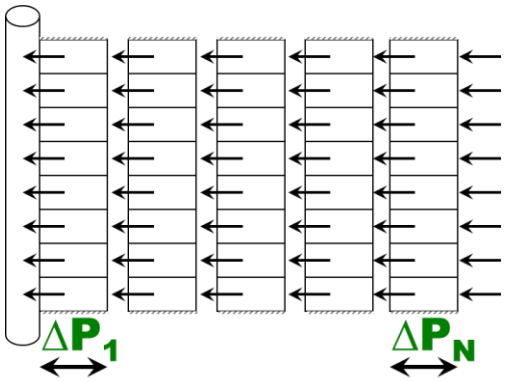

Figure 5: 2D Arithmetic-Harmonic average (King 2011)

- **2D/3D Incomplete layer method:** It uses the geometric average of the rigorous analytical upper (Arithmetic-Harmonic average) and lower (Harmonic-Arithmetic average) bounds (**Figure 6**).

$\bar{k} = \sqrt{k_{max} k_{min}}$ ... ... (1.5)

where,

k_{max} , average permeability from arithmetic-harmonic average, md;

k_{min}, average permeability from harmonic-arithmetic average, md;

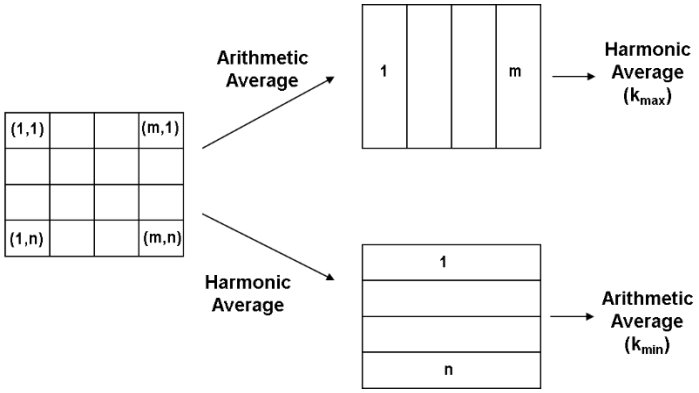

Figure 6: Incomplete layer method (Kelkar and Perez (2002))

- **Percolation theory**: It deals statistically with the problem of communication across complex systems constituted by objects that may or may not be connected. The critical point at which flow happens is called the percolation threshold. In the context of equivalent permeability, percolation theory is applied to materials with two phases, one of which is non permeable. For example, in **Figure 7,** consider all permeability below a threshold to be non-flowing and decrease the

threshold until the percolation threshold is reached to give the equivalent permeability of the block. This approach works best for large models with many flow paths (Ambegaokar et al. 1971).

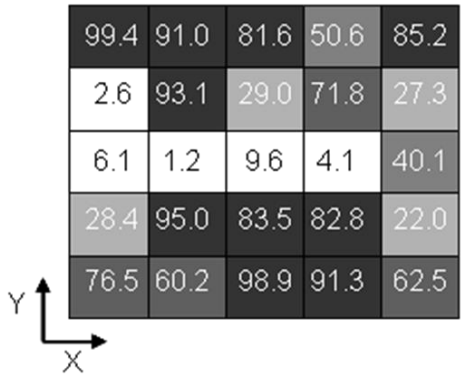

Figure 7: Percolation theory

- **Effective medium theory**: The heterogeneous medium constituted by homogeneous blocks side by side is replaced by a single inclusion of k permeability embedded in a homogeneous matrix with an unknown permeability k^0 and flow is constant around the embedded material. If the inclusion has a simple form, there is an analytical solution for the hydraulic head field inside and outside it, otherwise this approach is implemented numerically by allowing boundary conditions to be imposed at infinity reducing the impact of boundary conditions on the effective property.
- **Streamlines**: Streamlines are used to calculate the vertical permeability of the binary sand-clay system. The upscaled permeability is obtained by calculating

the head losses along a tortuous tube circulating inside the sand matrix. An improvement on this method is obtained by incorporating statistical parameters on the size and number of clay inclusions and generalizing it to stratified media. The resulting equation for vertical permeability is given by

$$k_v = \frac{(1 - F_s)h^2}{N_s \sum_{i=1}^{N_s} \frac{1}{S_i S_{ei}}} \dots\dots\dots\dots\dots\dots\dots\dots\dots\dots\dots\dots\dots\dots\dots\dots\dots\dots\dots\dots\dots\dots\dots\dots\dots\dots. (1.6)$$

where,

k_v, vertical permeability, md;

F_s, fraction of clay inclusions;

N_s, number of selected streamlines;

h, formation thickness; ft;

S_i, length of the i^{th} streamline; ft;

S_{ei}; length of the streamline weighted by the permeability; ft;

- **Renormalization**: It is a recursive algorithm in which effective permeability (k_{eff}) is determined by a series of successive aggregations using an electric network analogy to porous media (King 1989). A resistor network analogy used to write down direct expressions for k_{eff} on a sequence of 2x2x2 cells. It is a fast numerical calculation but less accurate than a non-recursive calculation.

1.1.2 Flow based upscaling methods

Begg et al. (1989) have shown that flow based upscaling techniques yield more accurate upscaled models compared to analytical techniques. In flow based upscaling, the steady state diffusion equation is solved numerically with linearly varying pressure field and specified pressure and flux boundary conditions.

Flow based upscaling can be either single phase or two phase. In two phase upscaling, the two-phase flow parameters such as relative permeability, fluid saturation, are also upscaled (Darman et al. 2002; Pickup and Sorbie 1996) in addition to the absolute permeability that is upscaled in single phase calculation. Two-phase upscaling is rarely used due to high computation cost involved in determining the upscaled relative permeability and the dependence of the resulting relative permeabilities on flow rates and well spacing (Barker and Thibeau 1997).

Farmer (2002) classified flow based upscaling into different types based on the two stage-upscaling procedure. In the first stage, a fine grid experiment is performed where one or more fine grid problems are solved which may include a single fine scale solution over the entire domain in each co-ordinate directions. If a single fine grid experiment covers a substantial part of the domain, the experiment is said to be global and if the single fine grid experiment covers only a one or more coarse grid cells at a time, then the calculation is said to be a local calculation. The second stage is called the coarse grid calibration stage where the fine grid solutions are used to determine the coarse scale

properties like permeability, k. When the calibration occurs locally on one or two coarse cells, it is described as local, otherwise the calibration is said to be global.

A classification is thus defined, where the first word refers to the fine grid experiment and the second word refers to the coarse grid calibration.

- **Local-Local upscaling:** In this type of upscaling, pressure boundary conditions are specified on the face edges of the coarse cell in one direction while all the other side boundary conditions may be linear pressure boundary conditions(King et al. 1998; King and Mansfield 1997), no-flow boundary conditions or periodic boundary conditions (Durlofsky 1991). **Figure 8** shows the 2D illustration of the upscaling method with an upstream pressure, p_{in} at the left edge and a downstream pressure, p_{out} at the right edge of the coarse cell and the side boundary conditions are no-flow. The flux, q is obtained from the steady state solution of the diffusion equation by solving for the unknown fine cell pressures numerically with the specified upstream and downstream pressures and side boundary conditions. The effective permeability is obtained from Darcy's law using **Eq. 1.7.** The local calculation is repeated in three co-ordinate directions to get the diagonal effective permeability tensor. This method was first introduced by Warren and Price (1961) and extended by Begg et al. (1989).

$$k_{eff} = \frac{q\mu L}{A(p_{out} - p_{in})} \quad (1.7)$$

where,

k_{eff}, effective permeability of the coarse cell, md;

q, flux across the coarse cell, RB/day;

μ, viscosity, cp;

A, cross sectional area of the coarse cell, ft^2;

L, length of the coarse cell, ft;

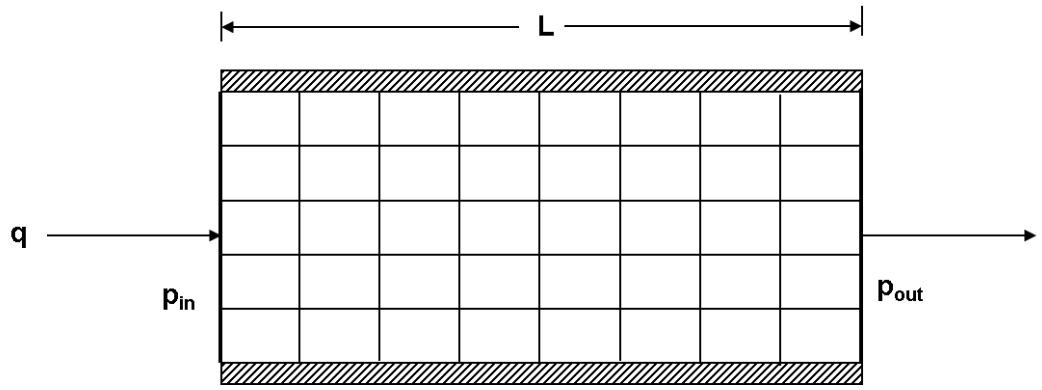

Figure 8: Local-local upscaling

In one dimension, the local-local permeability upscaling methods are exact but in 3D, the results depend on the choice of side boundary conditions (no-flow, periodic or linear). Holden and Nielsen (2000) have shown the non-uniqueness of local upscaling methods and their dependence on the choice of side boundary conditions. Some authors (Gomez-Hernandez and Journel 1994) have considered expanding the computation region beyond the region of interest by adding a skin region to the coarse cell so that ambiguity in boundary conditions is moved away

from the flow region (**Figure 9**). The average permeability is determined only using the region of interest. Larger the skin, higher would be the computation time of the calculation. Therefore, skin may be introduced only in directions transverse to the flow to optimize the performance. King (2007) advocated the use of extended local or wide boundary conditions as it less expensive than adding skin to the local region.

The non-uniqueness of the results can be minimized by performing an upgridding error analysis prior to upscaling to minimize the heterogeneity within the upscaling region.

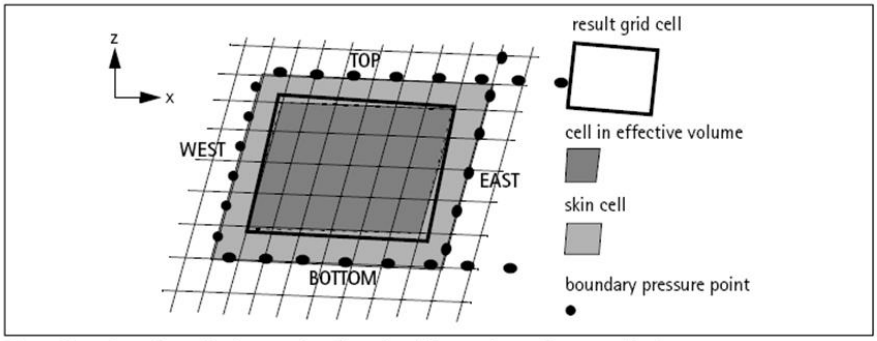

Figure H.9: Rescaling with the use of a skin region. (Picture shows direct sampling)

Figure 9: Adding skin region in local-local upscaling (RMS 2012)

- **Global-Local upscaling**: This method is applicable when an exact solution, or at least a good approximation, of the fine scale problem is available over most of the fine grid domain. One technique is to use the integrated fine flux over the

face of the coarse cell and use this information to calibrate a local solution on the coarse cell.

- **Global-Global upscaling:** This type of upscaling procedure minimizes a function measuring the difference between fine and coarse solutions which is computationally very expensive. The procedure is similar to history matching but here, a fine scale solution is used instead of physical measurements (Hales 1983; Tan 1995).
- **Local-Global upscaling**: It involves upscaling a fine model to small sub regions and interpolating the boundary conditions to construct the coarse grid properties. The purpose of this approach is to improve the upscaled dynamic parameters by adding a "border" (skin) region to better approximate the boundary conditions (Wen et al. 2005). It is an iterative approach with the following steps:
    1. Find the first guess solution of the coarse grid properties using a local-local upscaling method.
    2. Compute the skin zone boundary pressures from the upscaled values using interpolation.
    3. Upscale the coarse properties again using the interpolated skin zone boundary pressures.
    4. Compare values from 1&3. If significantly different, update and iterate.

If the knowledge of actual position of wells is known, the well flow rates may be specified to build a global flow pattern and utilize an iterative global solution on

the coarse grid to provide local boundary conditions for the upscaling calculation including the transverse pressure drop (Durlofsky 2005). This approach is called upscaling within the simulator as the global dynamic flow patterns are known from the position of wells.

- **Near Well Scale up:** This is an upscaling method which pays special attention to well blocks as the pressure drop near the well is radial and logarithmic compared to linear pressure drop elsewhere in the model. For each well, a single-well fine scale simulation is performed using an extended local upscaling method with bottom hole pressure ($p_{wf} = 1$) and boundary pressures set to 0 psi (**Figure 10**). The upscaled well block transmissibilities are computed by summing up fine scale cell flow rates and averaging fine cell pressures and the upscaled well index is computed using **Eq. 1.8** (Durlofsky et al. 2000)**.** The actual location of wells is needed for this method to be applicable which is not possible in the early stages of field life. Therefore, this method is useful when upscaling is done within the simulator.

$$WI = \frac{q_{wf}}{p_{wf} - \bar{p}_{wellblock}} \quad \ldots \ldots \ldots \ldots \ldots \ldots \ldots \ldots \ldots \ldots \ldots \ldots \ldots (1.8)$$

where,

WI, upscaled well index; RB/day/psi;

q_{wf}, well flow rate, RB/day;

p_{wf}, flowing bottom hole pressure, psi;

$\bar{p}_{wellblock}$, average well-block pressure, psi;

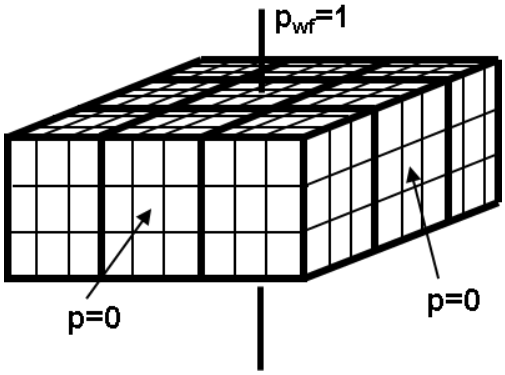

Figure 10: Near Well-Scale up (Durlofsky et al. 2000)

- **Well Productivity Index (PI) Upscaling:** King et al. (1998) proposed the well index upscaling method to preserve the flow between the wells and the reservoir. In this approach, three hypothetical directional wells (x, y, and z) are placed through the upscaled cell and the productivity of any physical well would be a weighted average of the three directional well productivities. The upscaled productivity of each directional well is the weighted average of directional well productivities through the fine grid. **Figure 11** illustrates the example for a vertical well productivity upscaling. The equations for directional well productivities are

$$\left(\sqrt{k_x.k_y}\right)^{Effective} = \frac{\sum_{ijk}\left(\sqrt{k_x k_y}.NTG.DV\right)_{ijk}}{\sum_{ijk}(NTG.DV)_{ijk}} \quad \text{(1.9.1)}$$

$$\left(\sqrt{k_y.k_z}\right)^{Effective} = \frac{\sum_{ijk}\left(\sqrt{k_y k_z.NTG}.DV\right)_{ijk}}{\sum_{ijk}\left(\sqrt{NTG}.DV\right)_{ijk}} \quad \text{(1.9.2)}$$

$$\left(\sqrt{k_x.k_z}\right)^{Effective} = \frac{\sum_{ijk}\left(\sqrt{k_x k_z.NTG}.DV\right)_{ijk}}{\sum_{ijk}\left(\sqrt{NTG}.DV\right)_{ijk}} \ldots\ldots\ldots\ldots\ldots\ldots\ldots\ldots\ldots\ldots\ldots\ldots (1.9.3)$$

where,

NTG, net to gross; fraction;

DV, bulk volume of the grid block; ft^3;

k_x, X direction permeability; md;

k_y, Y direction permeability; md;

k_z, Z direction permeability; md;

The average cell permeabilities can be obtained from the directional well productivities as shown below.

$$k_x^{Effective} = \frac{\left(\sqrt{k_x.k_y}\right)^{Effective}.\left(\sqrt{k_x.k_z}\right)^{Effective}}{\left(\sqrt{k_y.k_z}\right)^{Effective}} \ldots\ldots\ldots\ldots\ldots\ldots\ldots\ldots\ldots\ldots (1.10.1)$$

$$k_y^{Effective} = \frac{\left(\sqrt{k_x.k_y}\right)^{Effective}.\left(\sqrt{k_y.k_z}\right)^{Effective}}{\left(\sqrt{k_x.k_z}\right)^{Effective}} \ldots\ldots\ldots\ldots\ldots\ldots\ldots\ldots\ldots\ldots (1.10.2)$$

$$k_z^{Effective} = \frac{\left(\sqrt{k_x.k_z}\right)^{Effective}.\left(\sqrt{k_y.k_z}\right)^{Effective}}{\left(\sqrt{k_x.k_y}\right)^{Effective}} \ldots\ldots\ldots\ldots\ldots\ldots\ldots\ldots\ldots\ldots (1.10.3)$$

Using these permeabilities, the simulator can calculate the productivity of a physical well on the coarse cell which is equal to the averaged productivity of a

well with the same inclination on the fine scale. This method does not require the knowledge of rates or locations of the physical wells which will eventually be placed in the flow simulator. Therefore, the approach is significantly simpler to implement than the well flow based upscaling approaches.

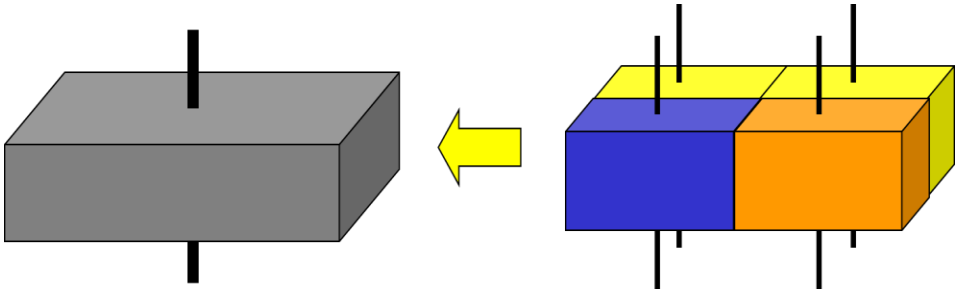

Figure 11: Well index upscaling method (King et al. (1998))

1.1.3 Permeability upscaling vs. Transmissibility upscaling

Several authors have published extensively on the permeability upscaling techniques (Durlofsky 2005; Farmer 2002; Gerritsen and Durlofsky 2005; Renard and de Marsily 1997; Wen and Gómez-Hernández 1996) where Darcy's law is used to compute the effective permeability which is proportional to the average fluid velocity. Romeu and Noetinger (1995) , King et al. (1998) and Chen et al. (2003) have shown that upscaling the inter-cell transmissibility rather than cell permeability is an effective way of upscaling the coarse simulation properties and yields more accurate results. Previous section has shown that the local upscaling calculations although cheap and fast, bias the answer depending on the choice of boundary conditions. Gomez-Hernandez and Journel

(1994) have suggested the use of a flow jacket or "skin" region around the coarse cell to move the ambiguity in boundary conditions away from the flow region which makes it an expensive calculation. Transmissibility upscaling on the other hand, is also a cheap calculation but doubles the spatial resolution of upscaling by capturing the fine scale juxtaposition of properties in the vicinity of a simulation cell face. Also, transmissibility is the term which goes directly into the difference equations of a finite difference reservoir simulator.

We focus on local transmissibility upscaling method where upscaling is centered at the simulation cell face instead of the cell itself, which corresponds to the inter-cell transmissibility used by the simulator. Zhou and King (2011) have shown a simple example highlighting the advantages of transmissibility upscaling over permeability upscaling. The author used well productivity upscaling to preserve the well flow rates and transmissibility upscaling to preserve the connectivity of the fine scale cells on the coarse grid. In **Figure 12**, the red dot represents a well which is in a continuous channel on fine scale. From permeability upscaling, a continuous channel is replaced by marginal sands and the highly productive well is replaced by a poor producer whereas transmissibility + well index upscaling preserves the barriers and productivity of the producing well. This example demonstrates the systematic bias introduced by permeability upscaling.

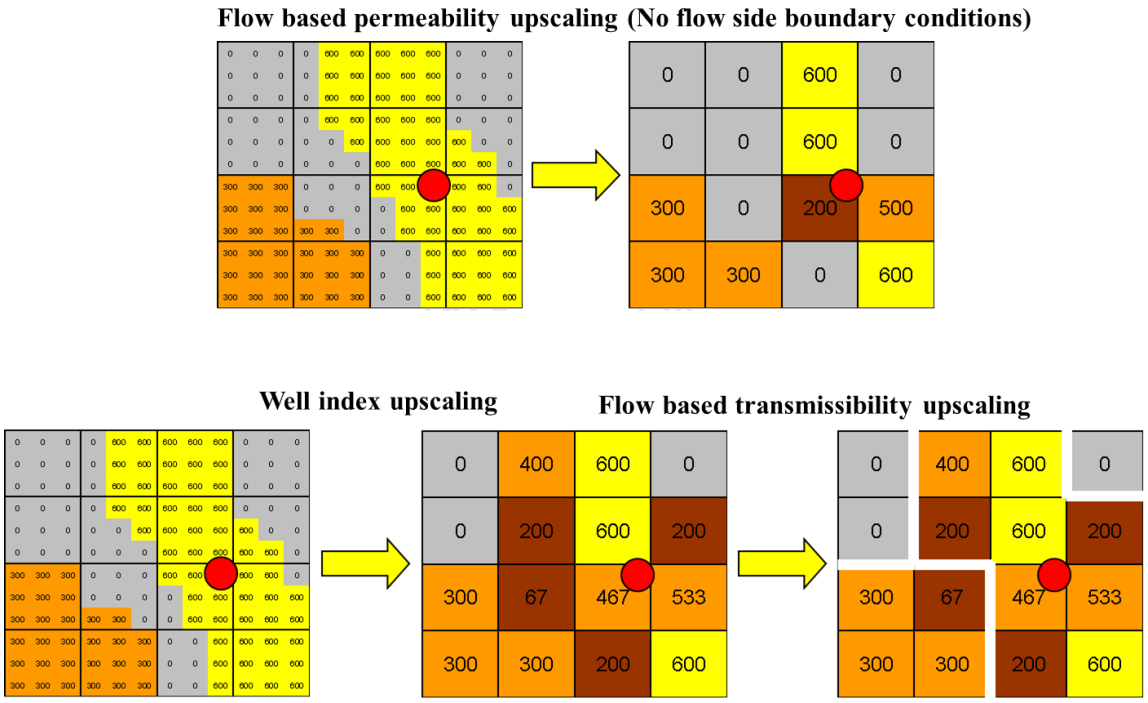

Figure 12: Permeability vs. Transmissibility upscaling (King (2007))

1.1.4 Multiscale upscaling methods

A critical underlying problem in reservoir modeling involves the need to resolve multi scale structure of the subsurface environment. While the length scales of geological features may be in millimeters, the simulation domain may be in the order of several kilometers. As a result, fully resolved numerical simulations are not feasible, yet the fine scale variations in the geologic model may affect the coarse grid solutions at all scales. Multiscale methods have been introduced as an alternative to standard upscaling techniques for incorporating detailed fine scale features at low computation cost.

In multiscale upscaling methods, the resolution of numerical simulation is improved on the coarse grid through some type of subgrid techniques (Efendiev and Durlofsky 2003). These techniques attempt to represent fine scale information on coarse scales in an indirect way. The pressures are solved on the coarse grid but fine-scale effects are captured through basis function determined from numerical solutions of local single phase flow problems on the underlying fine scale geologic model. The fine scale velocity is reconstructed using the basis functions.

Multiscale finite element methods (Hou and Wu 1997), multiscale finite volume method (Jenny et al. 2003) and multiscale mixed finite element method (Chen and Hou 2003) are among the relevant approaches for multiscale upscaling. Arbogast and Bryant (2002) proposed a variational multiscale approach formulated within the mixed finite element context where numerical Green's functions were used to resolve the fine scale information. Hou and Wu (1997) proposed the multiscale finite element method to capture the fine scale effects by constructing special finite element basis functions within each element but the reconstructed fine scale velocity was not conservative. Later, Chen and Hou (2003) proposed the conservative mixed finite element multiscale method.

Multiscale methods are out of scope for the current work. Therefore, they are not described in detail.

1.2 Simulation grid design

In this section, we review the importance of simulation grid design or upgridding in the reservoir modeling and simulation workflow. Upgridding studies are motivated by the desire to understand the errors introduced after an upscaling calculation or, equivalently an apriori upscaling error analysis is designed to identify the optimal coarsened resolution for the simulation grid. In the grid design, layer coarsening is the most important statistical problem as areal coarsening is typically constrained by well spacing constraints and CPU requirements.

The three important assumptions for upgridding and upscaling and their corresponding errors are summarized in **Table 1**. Each error is consistent with certain assumptions made on the coarse grid. Errors in pressure equilibrium are introduced when pay and non-pay cells are merged together in a coarse cell impeding the vertical connectivity. In this work, we will expand this simple statement and now treat the degree of connectivity using pressure transient concepts. The second error is introduced in multiphase flow where regions with high velocity variance will do a poor job in capturing the local spread in frontal velocity, while regions with minimal variance in local velocity preserve the fluid front in an upscaling calculation. This can be used as an error measure based on the variance in local velocity ($\frac{k}{\phi}$) proposed by King et al. (2006). Hosseini and Kelkar (2010) and Du (2012) extended the error measures by including the variance of local slowness ($\frac{\phi}{k}$) and a combined error measure which captures the variance of both ($\frac{k}{\phi}$) and

$(\frac{\phi}{k})$ in one estimate. The third error is introduced when the strength of off diagonal terms in the effective permeability tensor increase. This results in flow velocity being not aligned with the pressure gradient, which is difficult to capture using a two point flux approximation in the simulator.

Assumptions	Corresponding errors
Pressure equilibrium within one coarse cell	Disconnected pay within the coarse cell will not be in pressure equilibrium
Single velocity within one coarse cell	Distribution of multiphase frontal velocities are replaced by a single value
Fluid velocity is parallel to the pressure drop	Flow may depend on the transverse pressure drop

Table 1: Assumptions and their corresponding errors

In conclusion, connectivity, velocity variance, and off diagonal permeability elements may be used as grid diagnostics to design a simulation grid. Although, we are not doing an extensive literature review on upgridding, we stress the importance of an apriori upscaling error analysis for the design of simulation grid so that the heterogeneity of the fine scale model is best preserved on the coarse scale.

1.3 Scope of this work

The objective of this work is to extend the steady state local transmissibility upscaling methods to transient transmissibility upscaling. We use the Well Index upscaling proposed by King et al. (1998) to preserve the well productivity on the coarse grid. The methods developed for upscaling the inter-cell transmissibility are new.

Figure 13 illustrates the previously proposed steady state local transmissibility upscaling method (King 2007) in 2D. The left and right coarse cells are represented in yellow and green respectively. A planar pressure isobar of 1 psi is imposed as a boundary condition at the center of the left coarse cell and a 0 psi isobar at the center of the right coarse cell. The side boundary conditions are considered no-flow and the unknown pressures are solved using the steady state solution of the diffusion equation (**Eq. 1.11**) with the specified pressure and no-flow boundary conditions. The flux between the coarse cells can be obtained after solving the unknown fine scale pressures and the effective coarse cell transmissibility is obtained using **Eq. 1.12**. A fluid viscosity of 1 cp is used in all calculations.

$$\nabla.\left(\vec{\vec{k}}.\nabla p\right) = 0 \quad \ldots\ldots (1.11)$$

$$T_{eff} = \frac{q_{face}}{\Delta p} \quad \ldots\ldots (1.12)$$

where,

T_{eff}, effective transmissibility between the coarse cell, RB/day/psi;

q_{face}, flux between the two coarse cells, RB/day;

Δp, pressure drop between the two coarse cell centers, psi;

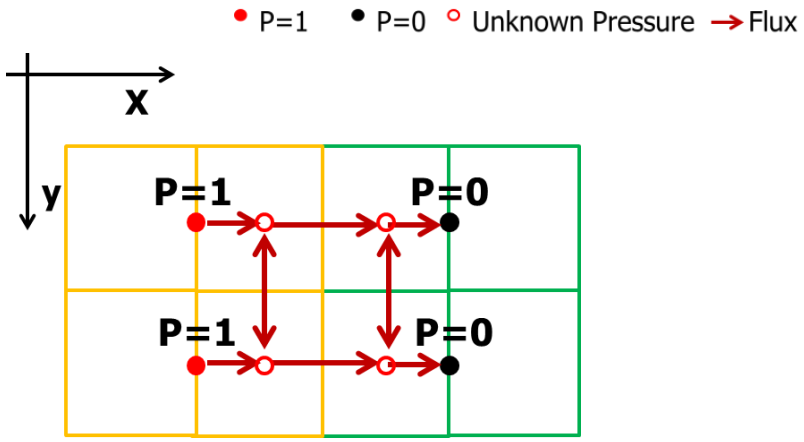

Figure 13: Steady state local transmissibility upscaling (King (2007))

Zhou and King (2011) used the steady state planar source and line source local transmissibility upscaling on a tight gas reservoir. The work has shown empirically that the half-cell planar source boundary conditions provide an upper estimate to the upscaled transmissibility the line source boundary conditions provide a lower estimate to the upscaled transmissibility.

Figure 14 illustrates the half-cell planar source and line source upscaling approaches. The pressure boundary conditions are introduced at the center of the coarse cells and the

steady state diffusion equation is solved with the specified boundary conditions to get the flux between the two coarse cells and in turn get the upscaled transmissibility which is nothing but flux per unit pressure drop. The side boundary conditions are considered to be no-flow.

Figure 15 illustrates the fine scale and upscaled cumulative recoveries of a sector model of a tight gas reservoir. The upscaled recoveries are obtained after 2x2 coarsening. Blue curve is obtained from the fine scale simulation, red curve is obtained from half-cell planar source upscaling and green curve is the result after line source upscaling. We can see the planar source upscaling was giving an upper bound and the line source upscaling was giving a lower bound to the cumulative gas recoveries compared to fine scale recovery. This result may be attributed to the ambiguity in the specification of the boundary conditions while upscaling the transmissibility.

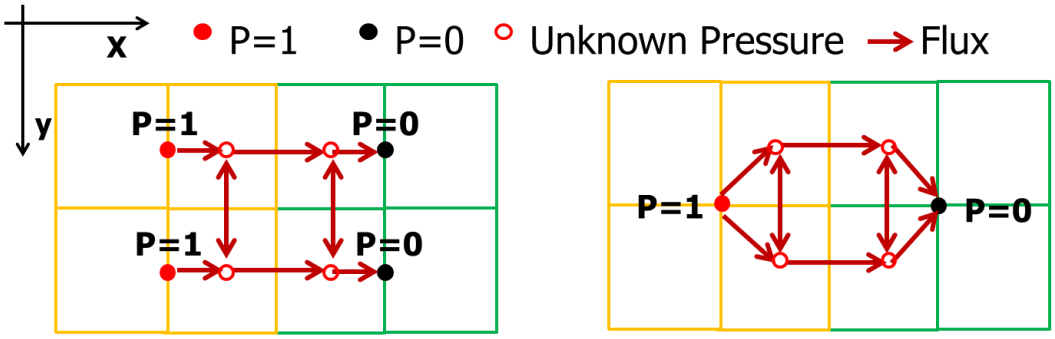

Upper Bound:
P=1 and P=0 along planar sources
No flow outer boundary conditions

Lower Bound:
P=1 and P=0 at cell nodes
No flow outer boundary conditions

Figure 14: Planar source vs line source upscaling (Zhou (2013))

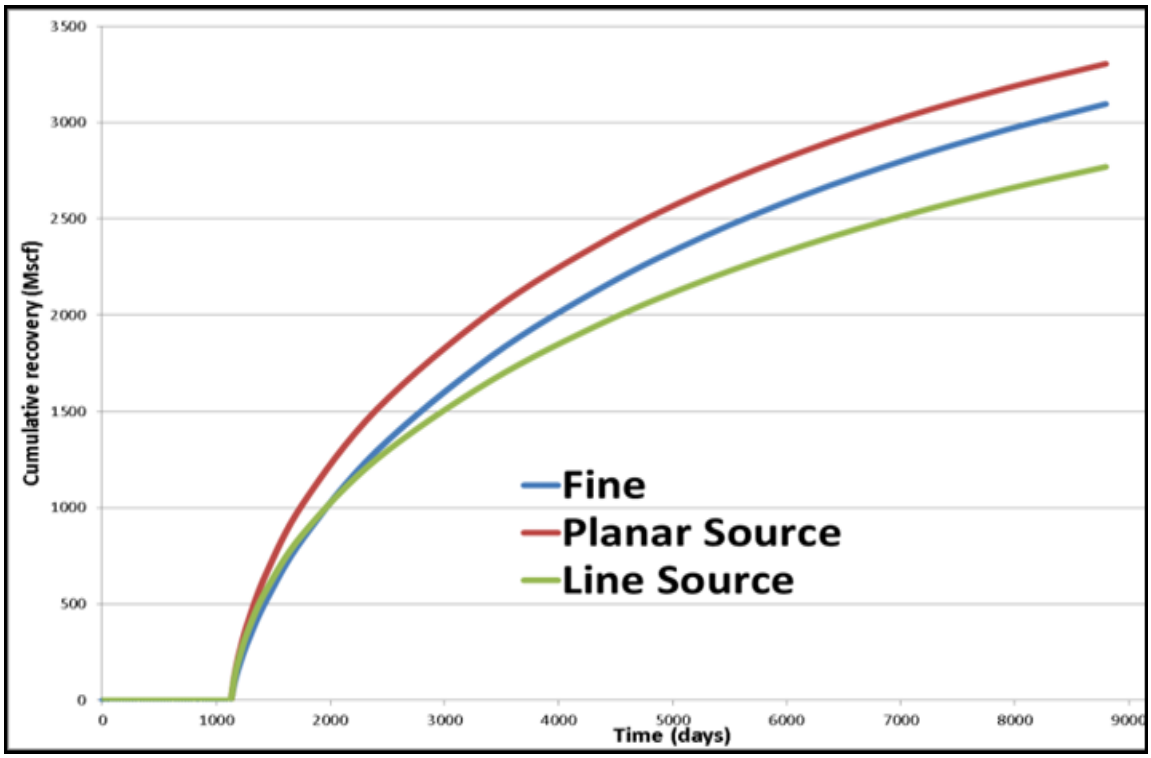

Figure 15: Steady state transmissibility upscaling

The current work intends to improve the results of the above mentioned steady state upscaling method by using drainage volume concepts to better capture the flow dynamics in tight systems.

CHAPTER II

DIFFUSE SOURCE TRANSMISSIBILITY UPSCALING

2.1 Motivation

The work done by Zhou and King (2011) in tight gas upscaling:

- Has shown empirically that the half-cell planar source boundary conditions provide an upper estimate to the upscaled transmissibility.
- Has shown empirically that the line source boundary conditions provide a lower estimate to the upscaled transmissibility.
- Has shown that the earlier attempt to implement a Pseudo Steady State (PSS) diffuse source upscaling algorithm encountered difficulties due to disconnected volume effects. We will discuss this method in detail as the work is not published.

2.1.1 Pseudo Steady State diffuse source upscaling

Zhou (2013) proposed a Pseudo Steady State (PSS) diffuse source algorithm in which the source/sink term in the diffusivity equation (**Eq. 2.1)** is considered without the time varying term.

$$\nabla . \vec{u} = \phi c_t \frac{\partial p}{\partial t} \quad \ldots\ldots (2.1)$$

The assumption here is the pressure drop w.r.t time in a coarse cell is in equilibrium within the cell and so is proportional to the pressure drop w.r.t time in all the fine cells that constitute the coarse cell **(Eq. 2.2)**.

$$\frac{\partial \bar{p}}{\partial t} = \frac{\partial p}{\partial t} \quad \ldots\ldots (2.2)$$

If we integrate the diffusivity equation (**Eq. 2.1**) with volume on both sides, we can see the right hand side volumetric source/sink term in each fine cell is proportional to its pore volume since the compressibility c_t and $\frac{\partial p}{\partial t}$ are constant (**Eq. 2.3)**.

$$\int \nabla . \vec{u}\, d^3x = c_t \frac{\partial p}{\partial t} \int \phi d^3x \quad \ldots\ldots (2.3)$$

The sum of source/sink terms of all the fine cells is the source/sink term of the coarse cell. In other words, the flux from the coarse cell (q_{face}) is the summation of fluxes of the fine cells (**Eq. 2.4**).

$$q_{face} = \frac{\int_{fine} q_{fine} \phi d^3x}{\int_{coarse} \phi d^3x} \quad \ldots\ldots (2.4)$$

Therefore, the average pressure in a coarse cell is the pore volume weighted average of fine cell pressures.

$$\bar{p} = \frac{\sum_i p_i PV_{\ i}}{\sum_i PV_i} \quad \ldots\ldots (2.5)$$

The author used geometric pressure approximation proposed by Xie et al. (2012) to modify the volumetric source/sink term in the diffusivity equation and set up the upscaling calculation (**Eq. 2.6**).

$$c_t \frac{\partial p}{\partial t} = -\frac{q_w}{V_p(r)} \quad \dots \quad (2.6)$$

where,

q_w, well flow rate, RB/day;

$V_p(r)$, Drainage volume; ft^3;

Let us consider a 1D example to summarize the approach. **Figure 16** shows the upscaling of linear flow from four cells to two cells. Cells 1, 2 and 3, 4 are merged.

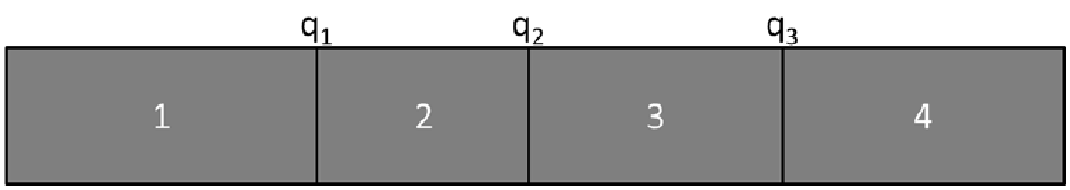

Figure 16: Upscaling linear flow from four cells to two cells (1+2 and 3+4)

The average pressure equations for the left and right coarse cell are:

$$p_{left} = \frac{p_1 PV_1 + p_2 PV_2}{PV_1 + PV_2}; p_{right} = \frac{p_3 PV_3 + p_4 PV_4}{PV_3 + PV_4} \quad \dots \quad (2.7)$$

where,

p_{left}, average pressure in the left coarse cell; psi;

p_{right}, average pressure in the right coarse cell; psi;

PV, pore volume of the fine cell; ft^3;

The diffuse mass conservation equations for the four fine cells are given below in their respective order.

$$q_1 = T_{12}(p_1 - p_2) = q_{face}\frac{PV_1}{PV_1 + PV_2} \quad (2.8)$$

$$q_2 = T_{23}(p_2 - p_3) = q_{face} \quad (2.9)$$

$$q_3 = T_{34}(p_3 - p_4) = q_{face}\frac{PV_4}{PV_3 + PV_4} \quad (2.10)$$

where,

q_{face}, flux between the coarse cells; ft^3/day;

T, inter-cell transmissibility; ft^3/day/psi;

PV, pore volume; ft^3;

The solution of the above equations is given below:

$$p_1 = p_{left} + \frac{PV_2}{PV_1 + PV_2}\frac{q_1}{T_{12}}; p_2 = p_{left} - \frac{PV_1}{PV_1 + PV_2}\frac{q_1}{T_{12}} \quad (2.11)$$

$$p_3 = p_{right} + \frac{PV_4}{PV_3 + PV_4}\frac{q_3}{T_{34}}; p_2 = p_{right} - \frac{PV_3}{PV_3 + PV_4}\frac{q_3}{T_{34}} \quad (2.12)$$

So:

$$\frac{q_{face}}{T_{23}} = p_2 - p_3 = p_{left} - \frac{PV_1}{PV_1 + PV_2}\frac{q_1}{T_{12}} - \left(p_{right} + \frac{PV_4}{PV_3 + PV_4}\frac{q_3}{T_{34}}\right) \ldots\ldots\ldots (2.13)$$

Or,

$$\frac{q_{face}}{T_{23}} = p_{left} - p_{right} - \frac{PV_1}{PV_1 + PV_2}\frac{q_1}{T_{12}} - \frac{PV_4}{PV_3 + PV_4}\frac{q_3}{T_{34}} \ldots\ldots\ldots\ldots\ldots\ldots\ldots\ldots\ldots (2.14)$$

By substituting the fluxes and average pressures in terms of q_{face} we have,

$$\frac{q_{face}}{T_{23}} = \frac{q_{face}}{T_{eff}} - \left(\frac{PV_1}{PV_1 + PV_2}\right)^2 \frac{q_{face}}{T_{12}} - \left(\frac{PV_4}{PV_3 + PV_4}\right)^2 \frac{q_{face}}{T_{34}} \ldots\ldots\ldots\ldots\ldots\ldots\ldots\ldots (2.15)$$

or,

$$T_{PSS} = T_{eff} = \frac{T_{23}}{1 + \left(\frac{PV_1}{PV_1 + PV_2}\right)^2 \frac{T_{23}}{T_{12}} + \left(\frac{PV_4}{PV_3 + PV_4}\right)^2 \frac{T_{23}}{T_{34}}} \ldots\ldots\ldots\ldots\ldots\ldots\ldots\ldots\ldots (2.16)$$

where,

T_{PSS}, Pseudo Steady State effective transmissibility between the coarse cells; ft^3/day/psi;

Now, consider the steady state homogeneous limit where all the cells have the same properties including the geometry i.e.

$$T_{12} = T_{23} = T_{34}; q_1 = q_2 = q_3 = q_{face}; PV_1 = PV_2 = PV_3 = PV_4 \ldots\ldots\ldots\ldots\ldots\ldots (2.17)$$

The steady state transmissibility would be

$$T_{SS} = \frac{T_{23}}{2} \ldots \ldots \ldots \ldots \ldots \ldots \ldots \ldots \ldots \ldots \ldots \ldots \ldots \ldots \ldots \ldots (2.17)$$

But, the Pseudo Steady State transmissibility is

$$T_{PSS} = \frac{2}{3} T_{23} = \frac{2}{3} T_{ss} \ldots \ldots \ldots \ldots \ldots \ldots \ldots \ldots \ldots \ldots \ldots \ldots (2.18)$$

We can see that the PSS transmissibility is off by a factor of 4/3 from the exact solution. The proposed pseudo steady state approach also failed in the presence of disconnected pay. **Figure 17** shows a two cell upscaling problem with regions of disconnected pay. If we apply the Pseudo Steady State upscaling here, we can see even though the volumes are disconnected from the inter-cell face, they would still have source/sink terms in the equation which leads to divergent pressure in the upscaling calculation as there is no exit path for the fluids in the disconnected volumes.

This is the motivation for us to consider transient approach to diffuse source upscaling. Before explaining the transient approach, we will give a brief background about the transient concepts we are using to set up the upscaling problem.

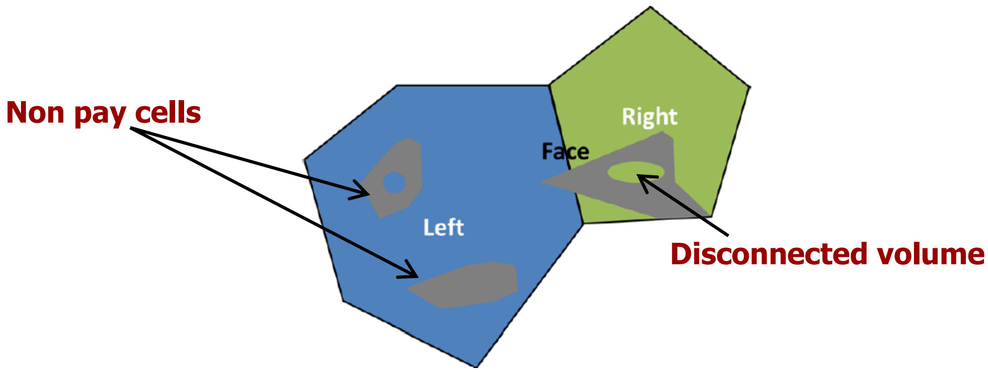

Figure 17: Two cell upscaling problem with regions of disconnected pay

2.2 Background

The radius of investigation represents the distance travelled by a pressure transient wave in a reservoir. Lee (1982) defined the radius of investigation as the distance of peak pressure disturbance from an impulse source or sink (**Eq. 2.19)**. For a 2D homogeneous reservoir:

$$r = \sqrt{\frac{kt}{948\phi\mu c_t}} \quad \ldots \ldots \ldots (2.19)$$

where,

r, radius of investigation (ft);

k, permeability (md);

t, time (hours);

ϕ, porosity (fraction);

c_t, total compressibility ($psia^{-1}$);

On the same lines, the concept of diffusive time of flight (τ) was introduced by Vasco et al. (2000) and Kulkarni et al. (2000) for heterogeneous reservoirs. τ represents the propagation time of pressure front in the reservoir. **Figure 18** illustrates the concept of diffusive time of flight in heterogeneous reservoirs where the contours of τ are shown compared to the contours of radius of investigation for homogenous reservoirs.

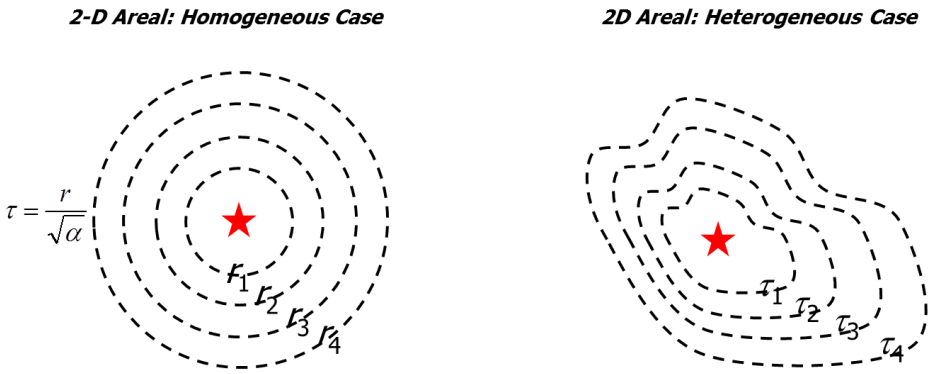

Figure 18: τ as a spatial coordinate (Datta-Gupta (2013))

The contours of τ can be obtained by solving the Eikonal equation (**Eq. 2.20**) which is a high frequency asymptotic solution of the diffusivity equation (Datta-Gupta and King 2007; Vasco et al. 2000).

$$\sqrt{\alpha(x)}|\nabla\tau(x)| = 1 \quad \ldots\ldots (2.20)$$

where,

$\tau(x)$, diffusive time of flight;

$\alpha(x)$ is the diffusivity given by

$$\alpha(x) = \frac{k(x)}{\phi(x)\mu c_t} \quad \text{(2.21)}$$

Eikonal equation tells us that the pressure 'front' propagates in the reservoir with a velocity equal to the square root of diffusivity. Diffusive time of flight along a ray path can be calculated using **Eq. 2.22**.

$$\tau(r) = \int_0^r \frac{1}{\sqrt{\alpha}}\, dr' \quad \text{(2.22)}$$

where,

r, distance from a source/sink;

We are using Dijkstra (1959) method for solving the Eikonal equation. The approach is explained in **Appendix A**. It is a single pass method and the solution can be constructed sequentially from small τ to large τ.

Xie et al. (2012) proposed a novel semi-analytical approach for the estimation of drainage volume, pressure and rate response without the need for a conventional numerical simulation. The author expressed the diffusivity equation in terms of drainage volume as shown below.

The diffusivity equation in radial form is given by

$$\frac{1}{A(r)}\frac{\partial}{\partial r}\left(\frac{k}{\mu}A(r)\frac{\partial p(r,t)}{\partial r}\right)=\phi c_t\frac{\partial p}{\partial t} \quad \ldots\ldots (2.23)$$

The Darcy flux is given by

$$q(r,t)=\pm\frac{kA(r)}{\mu}\frac{\partial p(r,t)}{\partial r} \quad \ldots\ldots (2.24)$$

Flux is inward for a producer and the sign is positive. For an injector, the flux is outward and the sign is negative. Combining **Eq. 2.23 & 2.24**, we obtain

$$c_t\frac{\partial p}{\partial t}=-\frac{1}{\phi A(r)}\frac{\partial q}{\partial r} \quad \ldots\ldots (2.25)$$

or,

$$c_t\frac{\partial p}{\partial t}=-\frac{\partial q}{\partial V_p(r)} \quad \ldots\ldots (2.26)$$

This development assumes that the pressure contours depend on r only, $p(r,t)$. The initial and boundary conditions are not described here. The extension of the above equations in heterogeneous τ coordinate are given below (**Eq. 2.27 & Eq. 2.28**).

$$c_t\frac{\partial p}{\partial t}=-\frac{\partial q}{\partial V_p(\tau)} \quad \ldots\ldots (2.27)$$

$$q=c_t\frac{dV_p}{d\tau}\frac{\partial p}{\partial \tau} \quad \ldots\ldots (2.28)$$

Xie et al. (2012) proposed a geometric pressure approximation of the **Eq. 2.27** yielding **Eq. 2.29**.

$$c_t \frac{\partial p}{\partial t} = -\frac{q_w}{V_p(t)} \dots\dots\dots\dots\dots\dots\dots\dots\dots\dots\dots\dots\dots (2.29)$$

The drainage volume $V_p(t)$ is obtained by evaluating the drainage volume $V_p(\tau)$ at the depth of investigation $\tau(t)$. However, the authors recognized that there was some ambiguity in this definition. Zhou (2013) proposed an improved geometric pressure approximation given by **Eq. 2.30**.

$$c_t \frac{\partial p}{\partial t} = -\frac{q_w}{V_p(t)} e^{-\frac{\tau^2}{4t}} \dots\dots\dots\dots\dots\dots\dots\dots\dots\dots\dots\dots (2.30)$$

where, the drainage volume, $V_p(t)$ is given by

$$V_p(t) = \int_0^{\infty} dV_p(\tau)\, e^{-\frac{\tau^2}{4t}} \cong \sum_i PV_i e^{-\frac{\tau_i^2}{4t}} \dots\dots\dots\dots\dots\dots\dots\dots\dots (2.31)$$

where,

PV, pore volume; ft^3;

The derivation for $V_p(t)$ is shown in **Appendix B**. So, the effective contribution of each grid block to the drainage volume varies with time as shown below where each fine cell's pore volume is discounted with the exponential weight.

$$PV_{i_{eff}} = PV_i e^{-\frac{\tau_i^2}{4t}} \dots\dots\dots\dots\dots\dots\dots\dots\dots\dots\dots\dots (2.32)$$

2.3 Pressure transient diffuse source upscaling

We are modifying the volumetric source/sink term in the diffusivity equation using the improved geometric approximation formulation proposed by Zhou (2013) (**Eq. 2.30**).

$$\nabla.\vec{u} = -\phi \frac{q_w}{V_p(t)} e^{-\frac{\tau^2}{4t}} \ldots\ldots\ldots\ldots\ldots\ldots\ldots\ldots\ldots\ldots\ldots\ldots\ldots\ldots\ldots\ldots\ldots\ldots\ldots\ldots\ldots\ldots\ldots\ldots\ldots\ldots (2.33)$$

The earlier approach starts with the Pseudo Steady State (PSS) limit of a pressure transient problem as a means of defining the diffuse source upscaling problem. In contrast to the earlier work, we will include the effects of transients and disconnected volumes. **Figure 17** illustrates how we are tackling the effects of disconnected volumes. Consider flux from left to right through the face shown. The pressure depletion in the left coarse cell is described by:

$$c_t \frac{\partial p}{\partial t} = -\frac{q_{Face}}{V_p(t)} e^{-\frac{\tau^2}{4t}}\, where\, V_p(t) = \int_0^\infty dV_p(\tau) e^{-\frac{\tau^2}{4t}} \ldots\ldots\ldots\ldots\ldots\ldots\ldots\ldots\ldots\ldots\ldots\ldots (2.34)$$

where,

q_{Face}, flux between the two coarse cells;

$V_p(t)$, drainage volume at the face;

τ is the diffusive time of flight measured from the flowing face to each fine cell, calculated using Dijkstra (1959) method. A potentially more accurate Fast Marching Method (Sethian 1999) may be used instead of Dijkstra’s, but this has not been found to be necessary for the current application. The equation for pressure increase in the right

cell is similar, with a change in sign for the flux. If $\tau(x, y, z)$ is finite, then we have a contribution to the drainage volume. On the other hand, if $\tau(x, y, z)$ is infinite, then $e^{-\frac{\tau^2}{4t}} \to 0$ and we have a disconnected volume. This will happened for zero permeability or regions bounded by zero permeability. So, we are effectively identifying the drainage volume from the face by considering the only those cells with finite values for τ.

2.3.1 Selection of time

Figure 19(a) shows the graphs of drainage volume of the coarse cell to the face vs time and the decay of drainage volume with time. We can see that the drainage volume increases rapidly, and then becomes almost constant with a decay rate dependent upon the largest finite τ. So, we choose a time at which the change in drainage volume is negligible w.r.t time. The expression for drainage volume is

$$V_p(t) = \sum_i PV_i e^{-\frac{\tau_i^2}{4t}} \quad \ldots\ldots (2.35)$$

Differentiating the above equation with time, we have

$$\frac{dV_p(t)}{dt} = \frac{1}{4t^2} \sum_i PV_i \tau_i^2 e^{-\frac{\tau_i^2}{4t}} \quad \ldots\ldots (2.36)$$

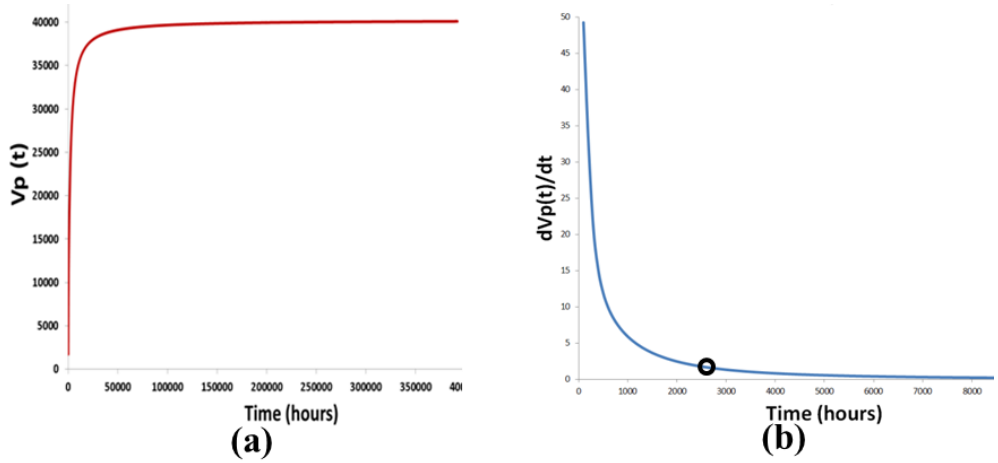

Figure 19: Selection of time (a): Drainage volume with time; (b): Drainage volume decay with time

We set a tolerance or a small value (0.0001 ft^3/hour) for $\frac{dV_p(t)}{dt}$ and determine the time for which $\frac{dV_p(t)}{dt} \leq$ tolerance. If we see the graph of $\frac{dV_p(t)}{dt}$ or the decay of drainage volume with time (**Figure 19(b)**), the black circle represents the time selected for the calculation. This time may be seen as the time close to the Pseudo Steady State (PSS) limit of the cells connected to the drainage volume at the face. If we use a bias variance methodology to set the tolerance, we would pick a point closer to the elbow in **Figure 19(b)**.

2.3.2 Example calculation

Let us consider a simple example to demonstrate the approach. **Figure 20** shows a 3x3 coarsening example in 2D with the grey cells being non pay.

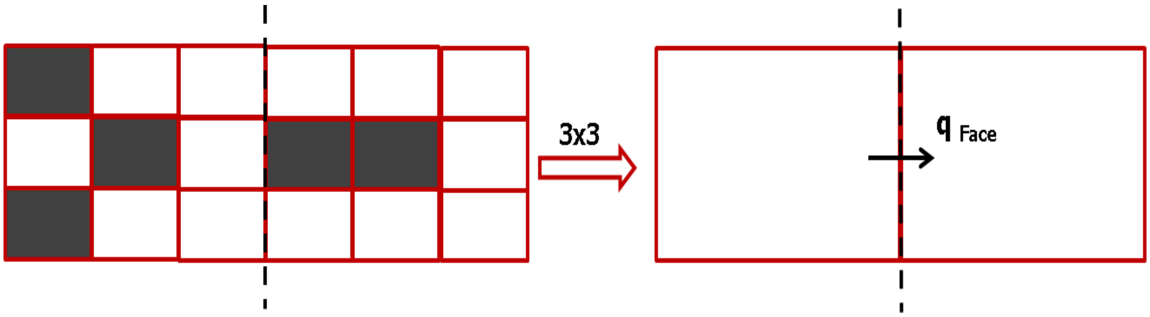

Figure 20: Diffuse source upscaling example

The effective transmissibility is given by

$$T_{eff} = \frac{q_{Face}}{< p_l > - < p_r >} \quad (2.37)$$

where,

T_{eff}, effective transmissibility between the two coarse cells; ft^3/day/psi;

$< p_l >$, average pressure of the cells connected to the face in the left coarse cell; psi;

$< p_r >$, average pressure of the cells connected to the face in the right coarse cell; psi;

The average pressures are given by the effective pore volume weighted average of fine cell pressures.

$$< p > = \frac{\sum_i p_i PV_i e^{-\frac{\tau_i^2}{4t}}}{\sum_i PV_i e^{-\frac{\tau_i^2}{4t}}} \quad (2.38)$$

Each fine cell connected to the face acts as a diffuse source/sink with the magnitude of the source/sink term proportional to $q_{Face} PV_i e^{-\frac{\tau_i^2}{4t}}$. The fine cells to the left of the

flowing face act as a diffuse source and the fine cells to the right act as a diffuse sink. So, we are effectively drawing fluids from the left coarse cell and injected them into the right coarse cell.

τ is the diffusive time of flight measured from the flowing face to the center of each fine cell using the Dijkstra (1959) method. Disconnected and non-pay cells have no contribution to the drainage volume since $\tau \to \infty$. Notice, the left most fine cell in **Figure 20** is disconnected from the drainage volume. The outer boundary conditions are considered no-flow making the diffuse source upscaling a purely local upscaling calculation.

Figure 21 is a 1D example that illustrates the diffuse source upscaling calculation.

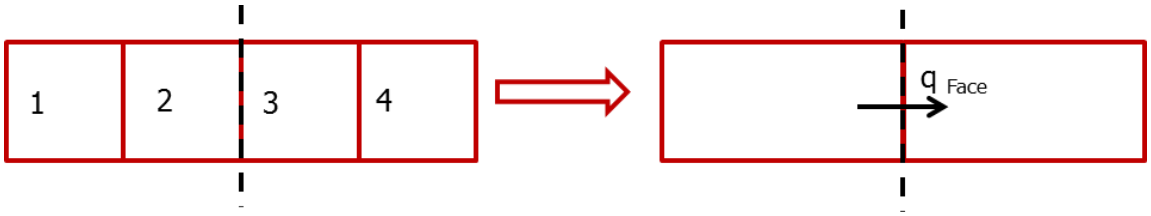

Figure 21: Diffuse source 1D example

Four fine cells are coarsened to two cells. The mass balance equations for the four cells are given below.

Cell 1: $T_{12}(p_1 - p_2) = \frac{q_{Face}}{V_{pleft}(t)} PV_1 e^{-\frac{\tau_1^2}{4t}}$ ..... (2.39)

Cell 2: $T_{12}(p_2 - p_1) + T_{23}(p_2 - p_3) = \frac{q_{Face}}{V_{pleft}(t)} PV_2 e^{-\frac{\tau_2^2}{4t}}$ ……(2.40)

Cell 3: $T_{23}(p_3 - p_2) + T_{34}(p_3 - p_4) = -\frac{q_{Face}}{V_{pright}(t)} PV_3 e^{-\frac{\tau_3^2}{4t}}$ ……(2.41)

Cell 4: $T_{34}(p_4 - p_3) = -\frac{q_{Face}}{V_{pright}(t)} PV_4 e^{-\frac{\tau_4^2}{4t}}$ ……(2.42)

Out of the four above equations, only three are independent. So, we add a gauge pressure condition setting the average pressure in the connected system to 0 psi.

$$\sum_i p_i PV_i e^{-\frac{\tau_i^2}{4t}} = 0 \text{ ……(2.43)}$$

The effective transmissibility is given by **Eq. 2.37** where the average pressures in the left and right coarse cells are given by **Eq. 2.44** and **Eq. 2.45**.

$$< p_l > = \frac{p_1 PV_1 e^{-\frac{\tau_1^2}{4t}} + p_2 PV_2 e^{-\frac{\tau_2^2}{4t}}}{PV_1 e^{-\frac{\tau_1^2}{4t}} + PV_2 e^{-\frac{\tau_2^2}{4t}}} \text{ ……(2.44)}$$

$$< p_r > = \frac{p_3 PV_3 e^{-\frac{\tau_3^2}{4t}} + p_4 PV_4 e^{-\frac{\tau_4^2}{4t}}}{PV_3 e^{-\frac{\tau_3^2}{4t}} + PV_4 e^{-\frac{\tau_4^2}{4t}}} \text{ ……(2.45)}$$

When calculating the effective transmissibility using **Eq. 2.37**, q_{Face} scales out of the problem as the average pressures are related to the fine cell pressures (p_1, p_2, p_3, p_4) as per **Eq. 2.44** and **Eq. 2.45** and the fine scale pressure are solved in terms of q_{Face}. This corresponds to solving the above equations with a unit flux i.e. $q_{face} = 1\ RB/day$.

CHAPTER III

FIELD APPLICATION

This chapter includes the details and results for field application of the diffuse source upscaling approach. The approach is tested on a US onshore tight gas field in Wyoming with 81 vertical wells and 24 years of depletion history.

3.1 Geological model description

The geological model uses a simple sand/non-sand facies description to represent the thin fluvial channels (**Figure 22(a)**). Non-net is defined using a permeability threshold, and was specified by the operator. The model size is 103x108x375 and the cells are 1 foot thick and 250 feet in length and breadth which means a very high vertical resolution compared to the areal resolution. Blue cells are pay; Red cells are non-pay making them inactive cells in the reservoir simulation. There are 693,154 active cells in the geological model. There is only intermittent connectivity in the fluvial sands.

Figure 22(b) shows the porosity distribution where most of the porosity of the model has a range between 0.10 and 0.15. **Figure 22(c)** shows the heterogeneous permeability distribution with permeabilities ranging from micro to milli-darcies. 70% of the pay cells have permeabilities above 0.1 md while the rest fall below 0.1 md.

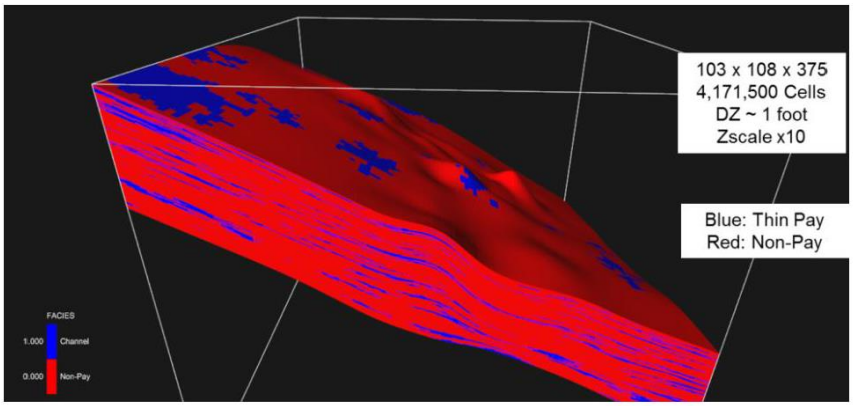

(a)

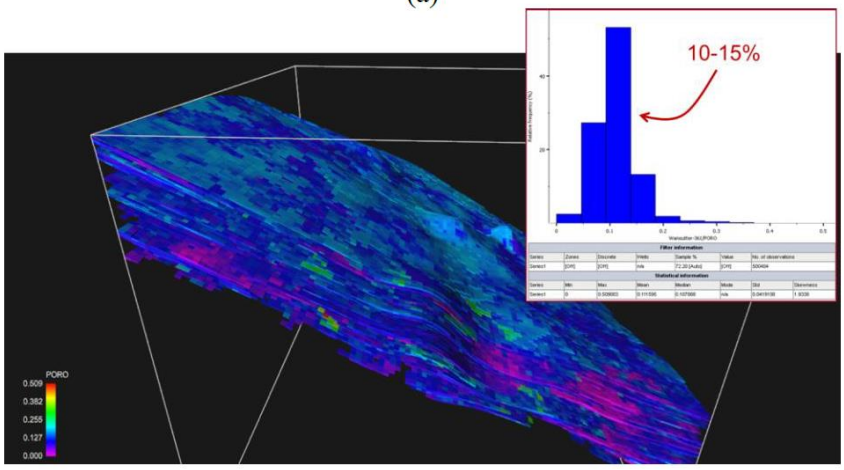

(b)

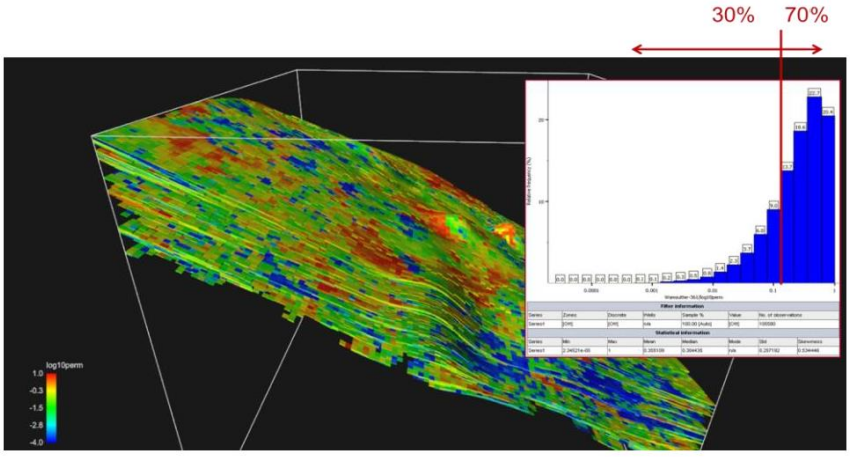

(c)

Figure 22: High resolution geologic model (a): Facies distribution; (b): Porosity distribution for the pay cells; (c): Permeability distribution for the pay cells

The geological model has 5 geological zones and 81 vertical producers with 24 years of pressure depletion history.

3.2 Adaptive upgridding (coarsening)

For a model with such high heterogeneity, preserving the channel flow path, barriers of non-pays and capturing the internal heterogeneity becomes a crucial factor in designing the simulation grid. We are using the adaptive upgridding approach proposed by Zhou and King (2011) where three different coarsening resolutions are chosen, 1x1xN, 2x2xN and 3x3xN. **Figure 23** illustrates the upgridding or the coarsening strategy we are using. For 1x1xN or pillar based coarsening (**Figure 23(a))**, everything is merged in the vertical direction until a barrier is hit so that vertical flow communication is preserved on the fine scale. This approach helps to keep pay and non-pay separate while coarsening so that there is pressure equilibrium within the coarse cell. For 2x2xN and 3x3xN coarsening (**Figure 23(b) and (c)**), both horizontal and vertical communication is considered when assessing continuity. **Figure 23(b)** shows an example of coarsening algorithm in which there is no vertical communication from top to bottom. Therefore, N would have a maximum value of 2 since a maximum of 2 layers can be merged as shown in the picture. As long as there is vertical communication across the entire sands, coarsening is performed as shown in **Figure 23(c)** where 3 layers are merged to get a single coarse cell. However, vertical communication does not guarantee horizontal communication. Coarsening in the areal direction can be dangerous as it may violate the

pressure equilibrium assumption in the coarse cells. Therefore, we can expect increased upscaling errors in areal coarsening approaches (2x2xN and 3x3xN).

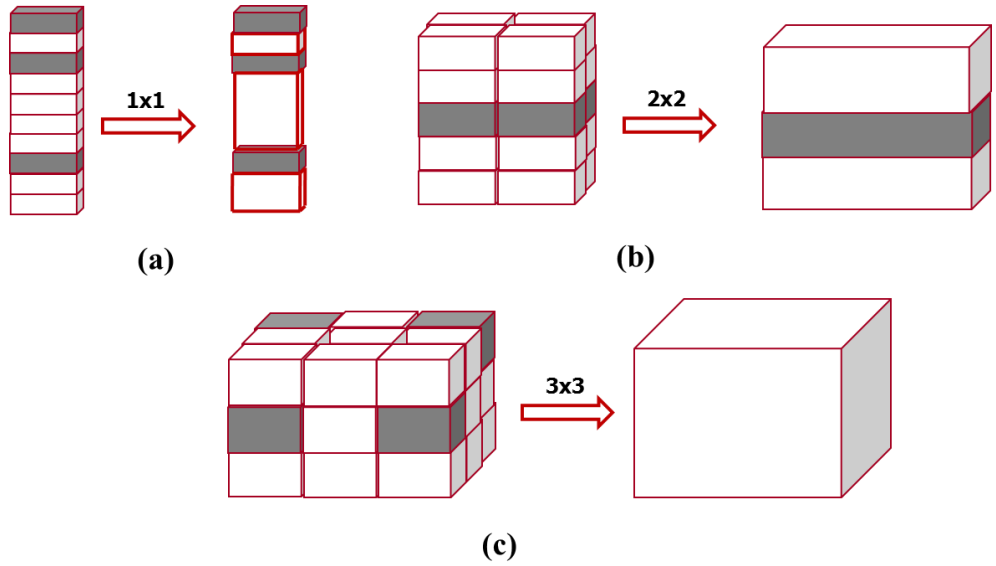

Figure 23: Adaptive upgridding for tight gas reservoirs (a): 1x1xN; (b): 2x2xN; (c): 3x3xN

3.3 Sector model results

The diffuse source upscaling approach is first tested on a sector model of size 10x10x375 with a single producer and 24 years of production.

Figure 24 shows the cumulative gas recoveries for 1x1xN upscaling with about a factor of four reduction in active cells. We can see an excellent agreement of coarse model recoveries with the fine scale recoveries being superposed on the coarse model recoveries. In 1x1xN case, planar source and line source are the same approaches and

they also yield an exact solution. The histogram at the bottom right shows the difference in coarse model pressures and the fine scale pressures at the end of simulation. We can see 95% of the coarse cells are below a difference of 0.5 psi compared to the fine scale pressures which suggests that all the coarse cells are in pressure equilibrium.

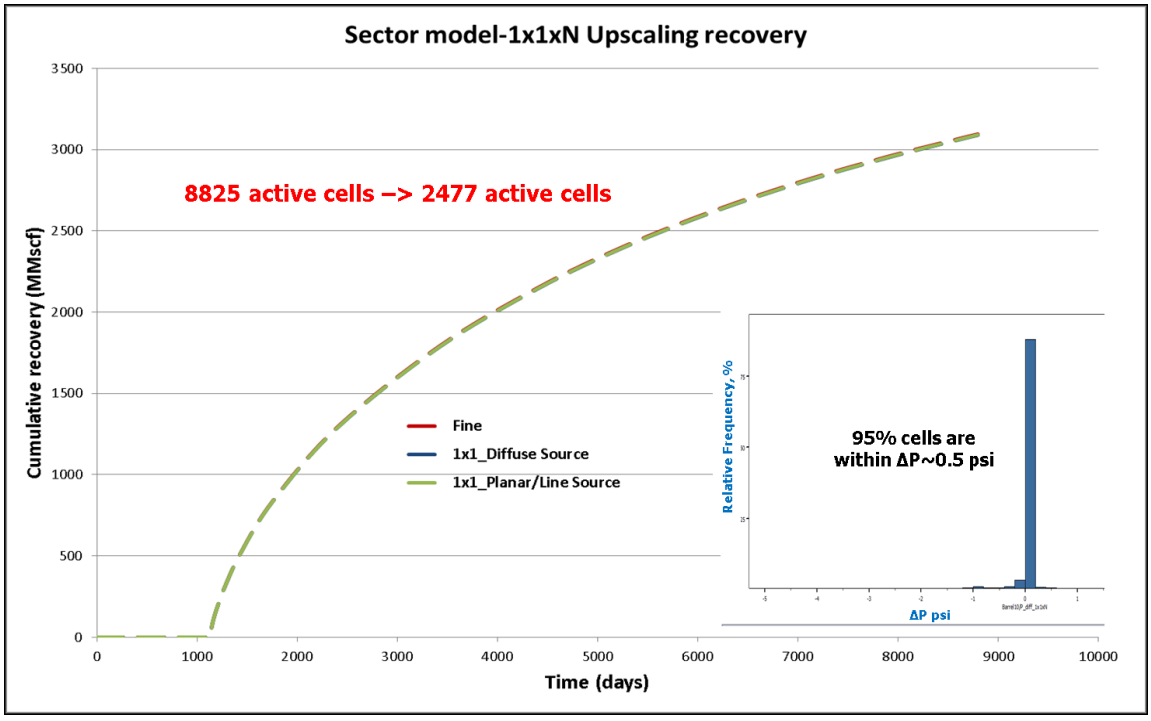

Figure 24: Sector model 1x1xN upscaling cumulative gas recovery

Figure 25 shows that the cumulative gas recoveries for 2x2xN upscaling with about a factor of ten reduction in the number of active cells relative to the fine scale model. Red curve is the fine scale recovery, the blue curve is the result obtained from planar source upscaling and the green curve is obtained from line source upscaling. While the previous two approaches were giving an upper bound and lower bound to the fine scale recovery,

diffuse source upscaling approach is able to match the prediction of fine scale recovery reasonably well with 80% of the coarse cells in the model below 2 psi difference from the fine scale pressures.

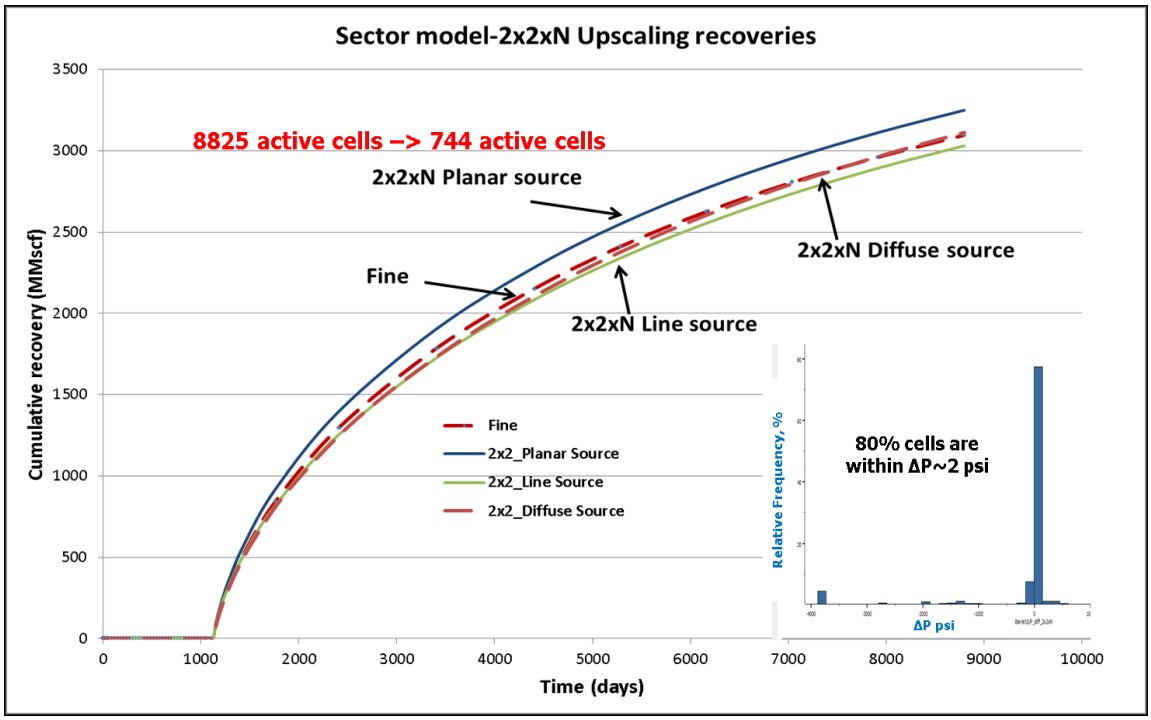

Figure 25: Sector model 2x2xN upscaling cumulative gas recovery

Figure 26 shows the result for 3x3xN upscaling which is a much aggressive coarsening with only 489 active cells in the coarse model compared to 8,825 active cells in the fine scale model. While the previously proposed approaches produced considerable errors in performance prediction, the diffuse source approach is able to get close to the fine scale recovery reasonably well even with only 489 active cells in the final coarse model.

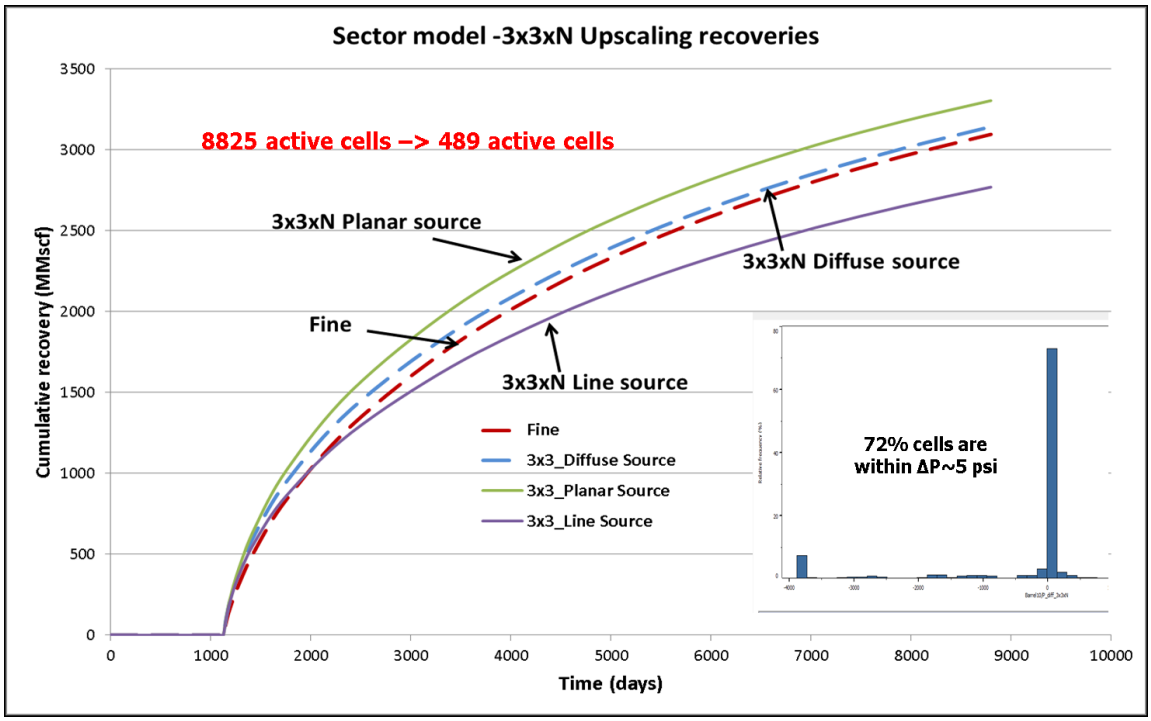

Figure 26: Sector model 3x3xN upscaling cumulative gas recovery

To validate the upscaling calculation further, we have also compared the pressure maps at the end of simulation. **Figure 27** shows the pressure maps for pillar based upscaling (1x1xN). The fine scale pressure map is at the left and the coarse model pressure map is at the right. We can see both are indistinguishable visually, which agrees well with the cumulative gas recoveries shown in **Figure 24**. **Figure 28** and **Figure 29** show the pressure map comparisons for 2x2xN and 3x3xN upscaling with a reduction in spatial resolution. Even with a much coarser resolution as shown in **Figure 29**, we can see a good visual match in pressures compared to the fine scale.

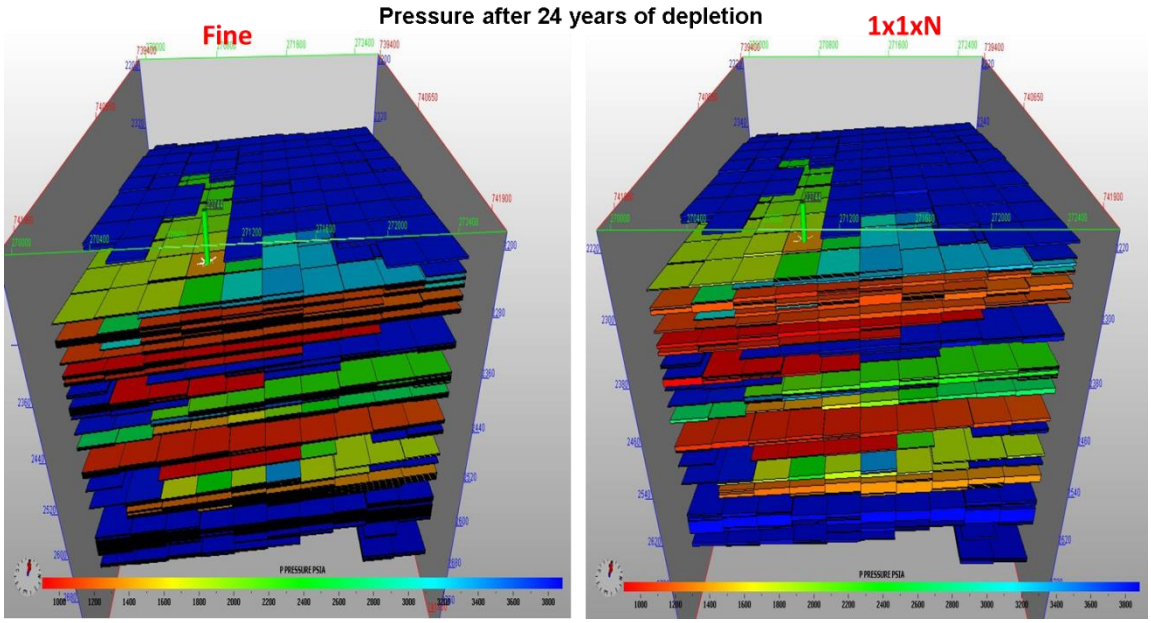

Figure 27: Sector model 1x1xN pressure map comparison

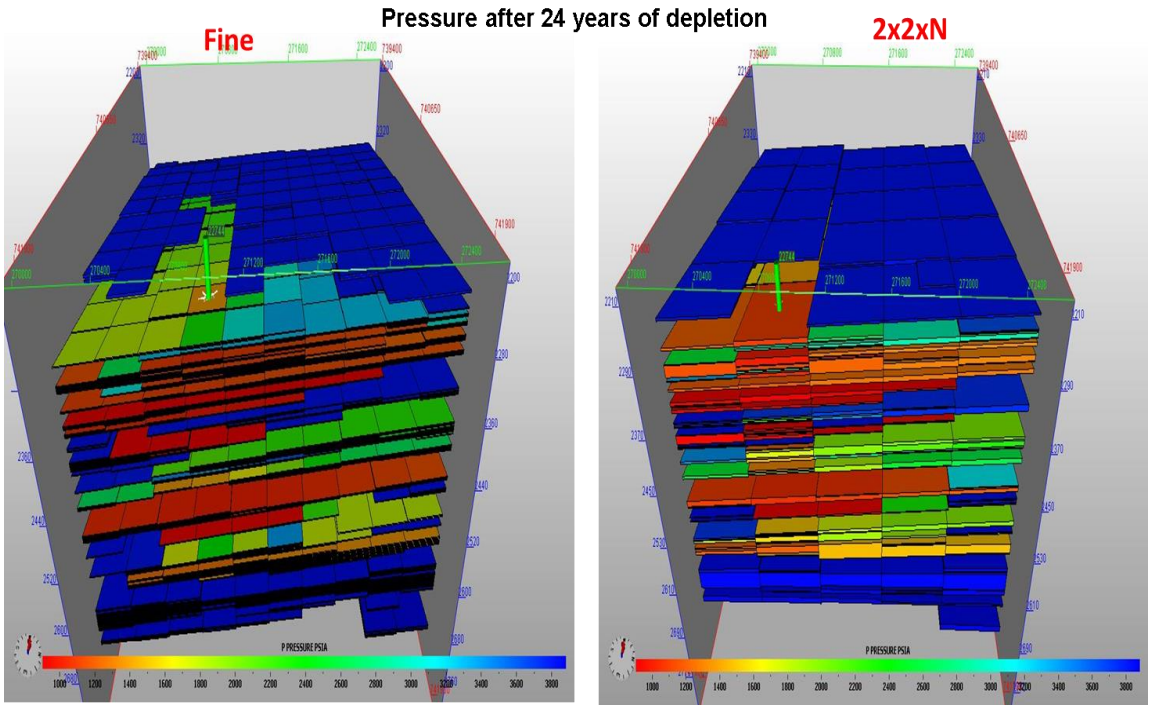

Figure 28: Sector model 2x2xN pressure map comparison

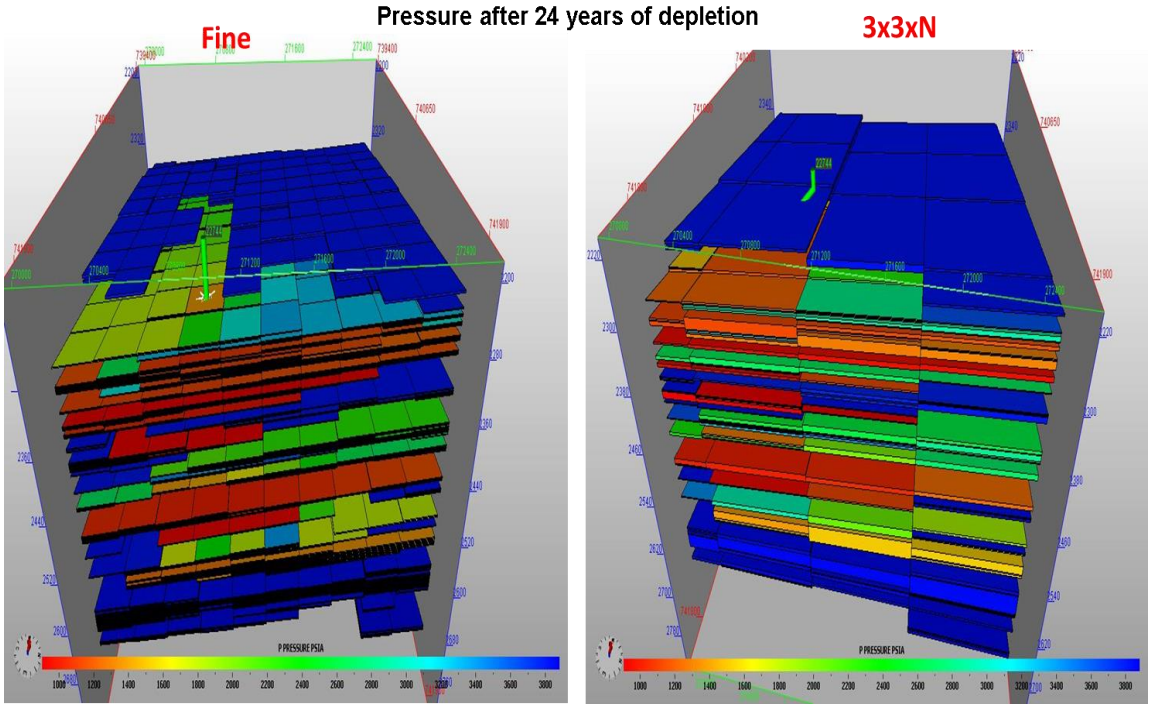

Figure 29: Sector model 3x3xN pressure map comparison

3.4 Full field model results

After getting positive results in the sector model upscaling, we tested the diffuse source upscaling approach on the full field model with around 4.2 million cells, 81 vertical producers and 24 years of pressure depletion. **Figure 30** shows the result for pillar based upscaling (1x1xN). We can see an accurate performance prediction even with only 234,565 active cells in the coarse model compared to 693,154 active cells on the fine scale. The pressure histogram also indicates excellent agreement with the fine scale model.

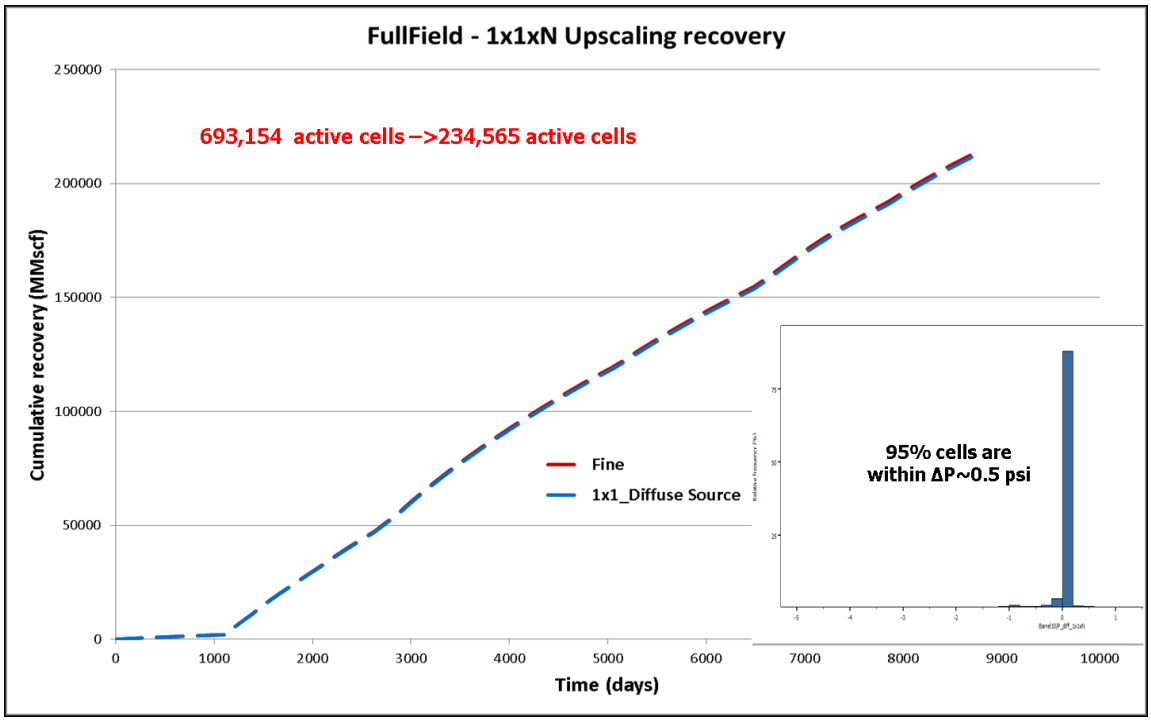

Figure 30: Full field model 1x1xN upscaling cumulative gas recovery

Figure 31 shows the results for 2x2xN upscaling where the previous approaches bounded the fine scale recovery, the diffuse source approach is able to predict the cumulative gas recoveries without much loss in accuracy. **Figure 32** shows the result for an aggressive coarsening with only 39,375 active cells in the coarse model. We can see a reasonable prediction of the cumulative gas recoveries compared to the other approaches. The histogram shows that 75% of the cells are within a pressure difference of 10 psi compared to the fine scale model.

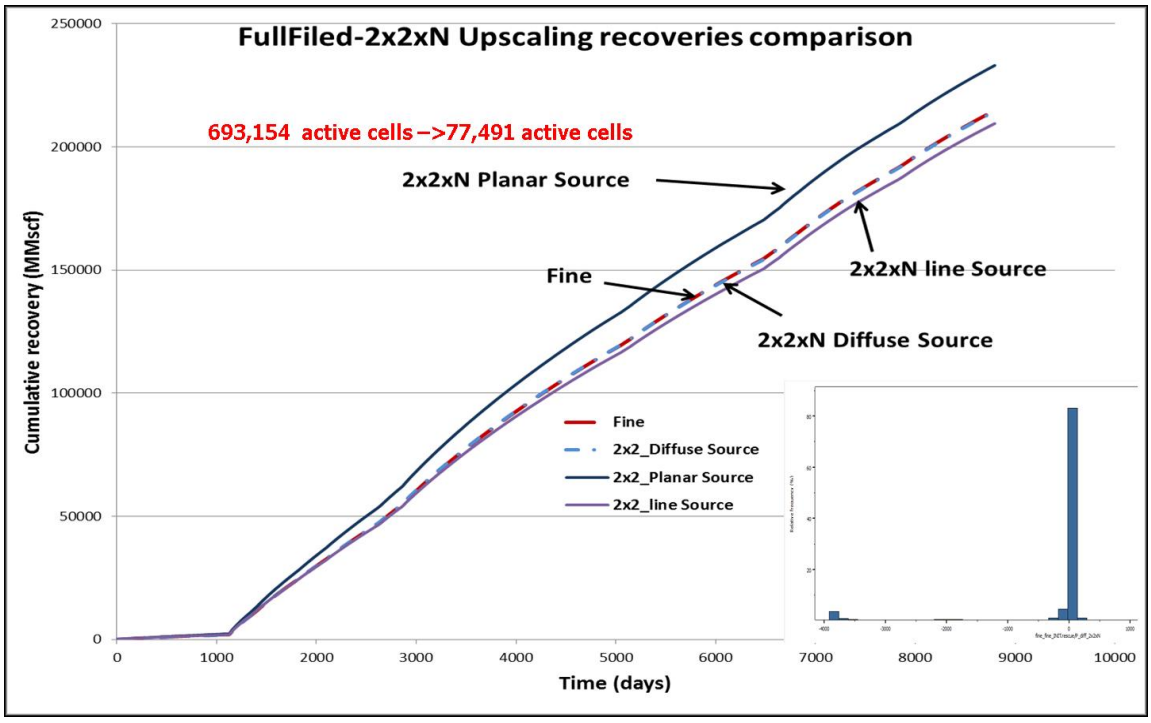

Figure 31: Full field model 2x2xN upscaling cumulative gas recovery

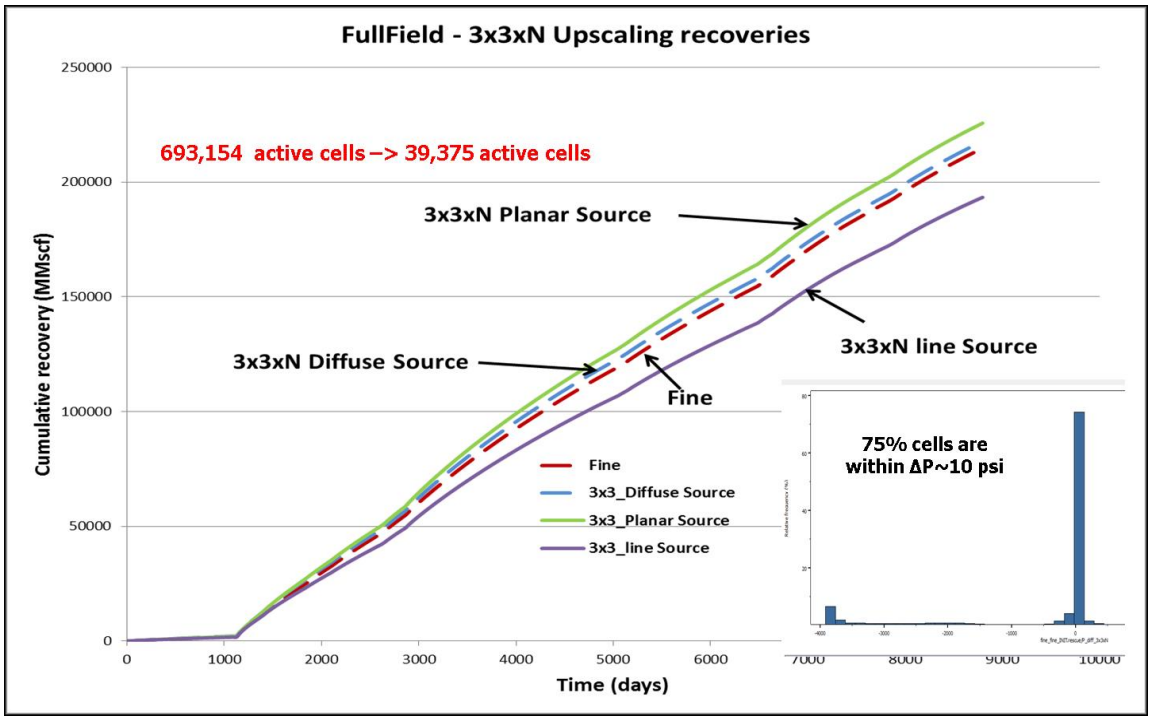

Figure 32: Full field model 3x3xN upscaling cumulative gas recovery

Figure 33, **Figure 34**, and **Figure 35** show the pressure map comparisons of the three coarsening approaches: 1x1xN, 2x2xN and 3x3xN respectively. The green pipes represent the wells in the model. The results are very much similar to the sector model results. All three coarsening approaches show a good visual agreement with the fine scale pressure map. **Figure 36** shows the graph of CPU time vs active cell count which scales linearly on the log-log graph. We have been able to reduce the CPU time by two orders of magnitude without significant loss in accuracy of performance prediction.

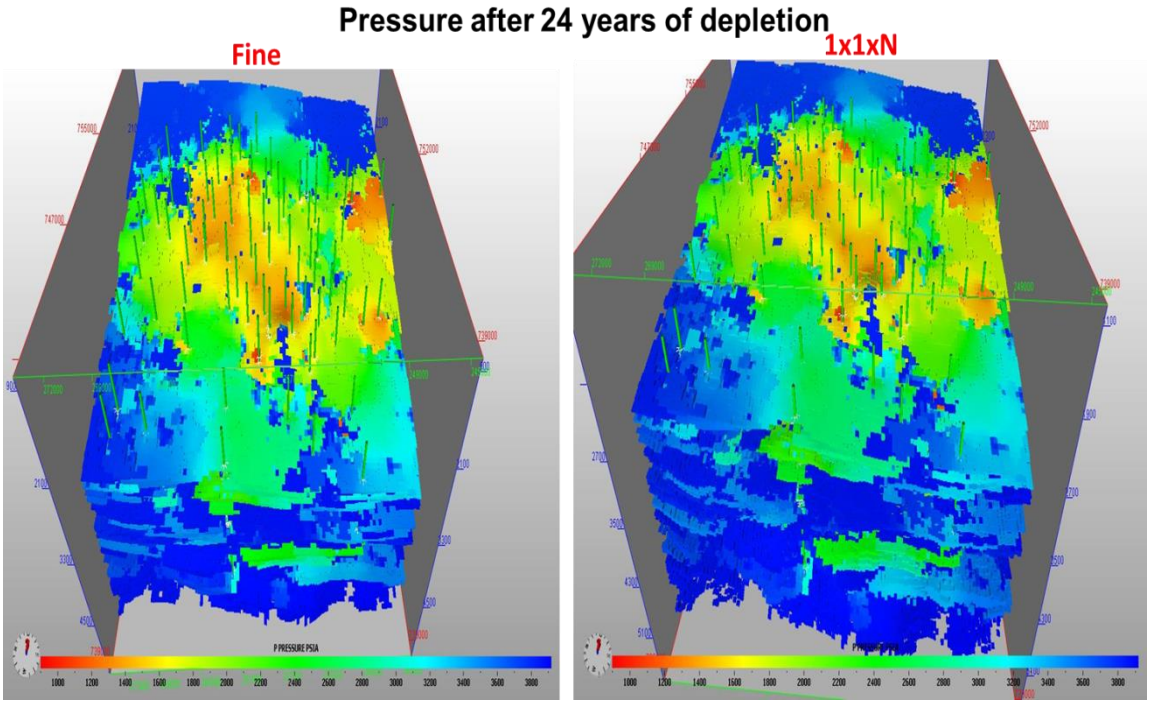

Figure 33: Full field model 1x1xN pressure map comparison

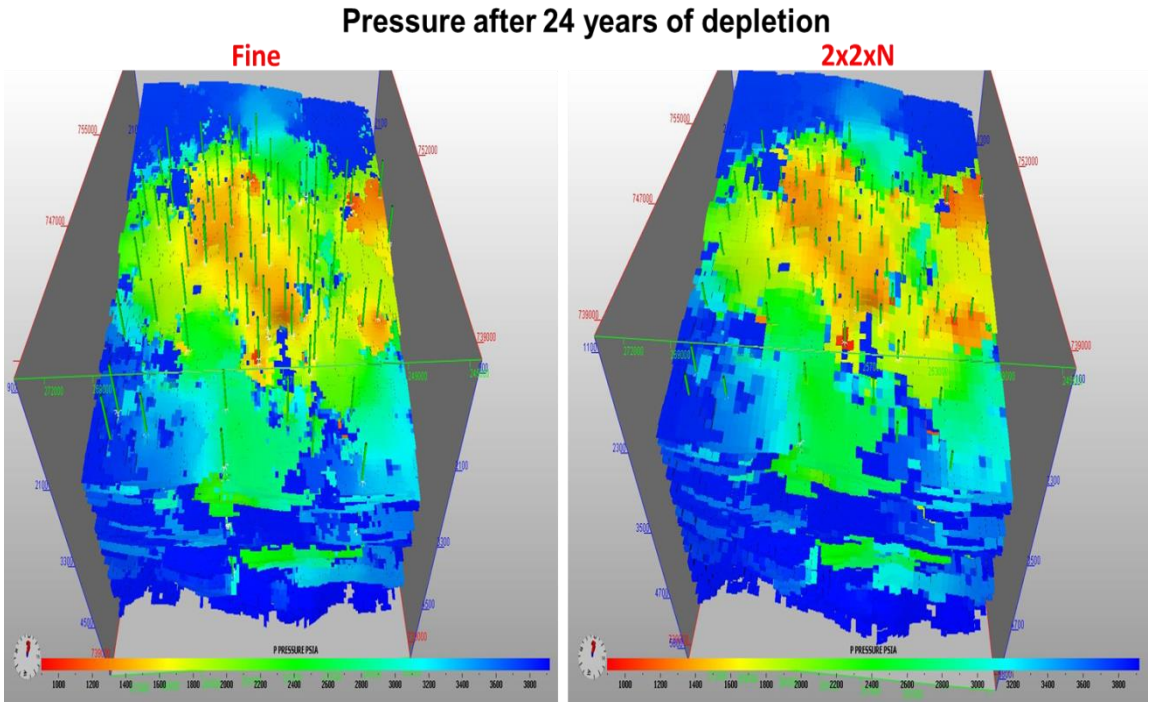

Figure 34: Full field model 2x2xN pressure map comparison

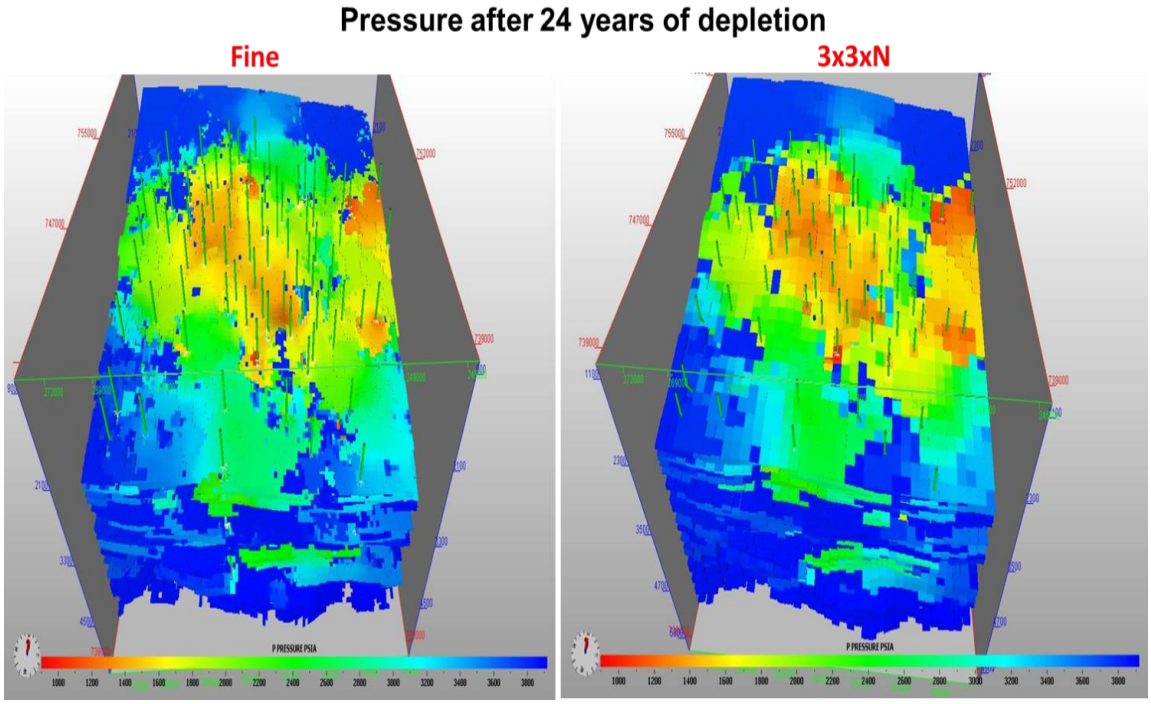

Figure 35: Full field model 3x3xN pressure map comparison

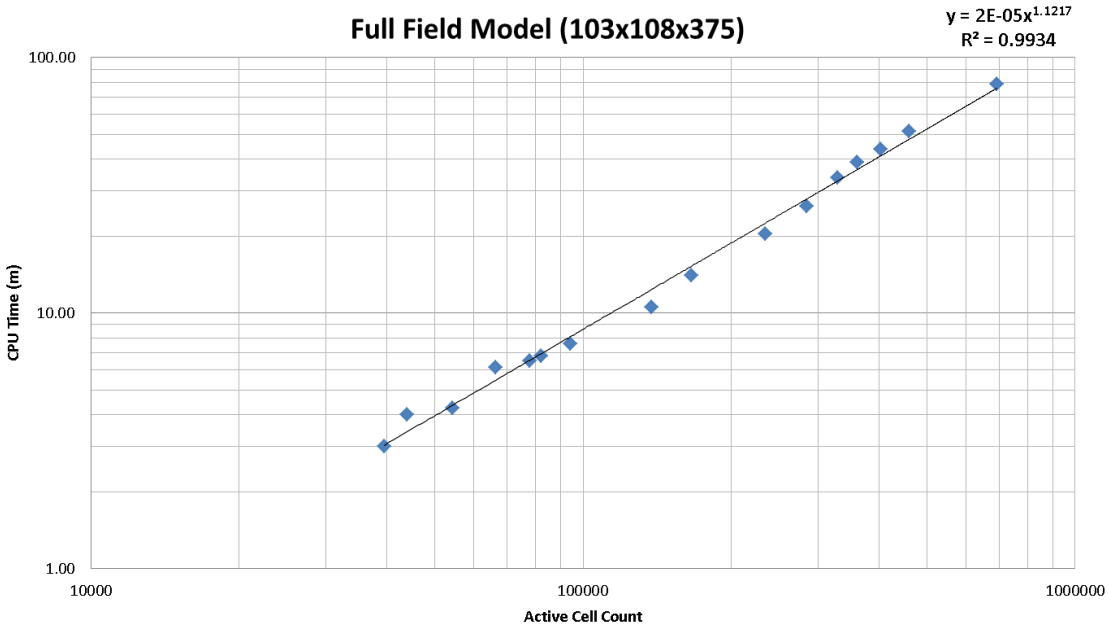

Figure 36: CPU time scaling behavior

CHAPTER IV

FUTURE RESEARCH

In this chapter, we discuss the areas where further investigation is needed with the proposed diffuse source upscaling algorithm.

4.1 Time threshold

The procedure where we set a threshold for decay of drainage volume with time in **Section 2.3.1** Selection of time is not general. Further investigation can help in generalizing the procedure for time thresholding so that the algorithm can be applied to other systems.

4.2 Spatial averaging of pressure

We are using a linear pore volume weighted average for calculating the average pressure in a coarse cell. But, the pressure follows a quadratic trend if we use the diffuse source upscaling algorithm rather than a linear trend which is seen in steady state. We will discuss this further with a simple homogenous example at a long time limit.

Figure 37 shows the velocity profile of a two cell homogenous case with a cross-sectional area A, length DX of each cell and flux, q_F between the cells. The outer

boundary conditions are no-flow. The velocity gradients in the left and right cell for the Pseudo Steady State (PSS) flow are given by **Eq. 4.1** and **Eq. 4.2**.

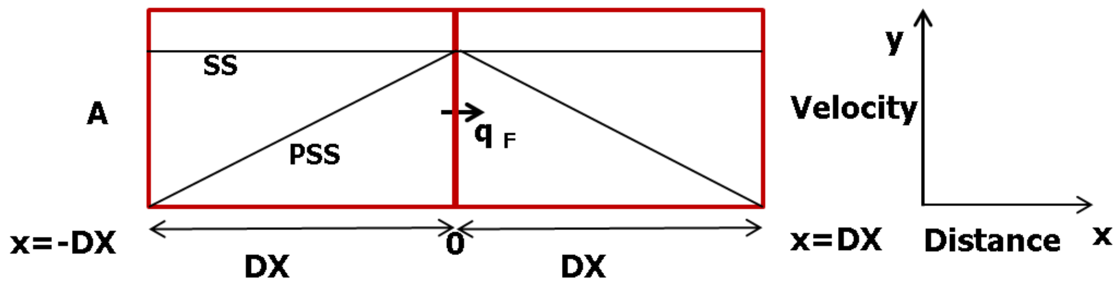

Figure 37: Velocity profile

$$\frac{\partial u_l}{\partial x} = \frac{q_F}{A.DX} \quad \ldots \ldots (4.1)$$

$$\frac{\partial u_r}{\partial x} = -\frac{q_F}{A.DX} \quad \ldots \ldots (4.2)$$

where,

u_l, velocity of the left cell; ft/day;

u_r, velocity of the right cell; ft/day;

q_F, flux between the cells; ft^3/day;

A, cross-sectional area; ft^2;

DX, length of the cell; ft;

Since the outer boundary conditions are no-flow, the velocity at the cell edges, x=-DX and x=DX is zero and the maximum at the inter-cell face, x=0. Using these boundary conditions, we can obtain the expression for velocities in each cell which are linear in x given by **Eq. 4.3** and **Eq. 4.4**. Notice that there is a constant velocity profile throughout the cells in the Steady State (SS) flow.

$$u_l = \frac{q_F}{A}\frac{DX + x}{DX} \quad \ldots\ldots (4.3)$$

$$u_r = \frac{q_F}{A}\frac{DX - x}{DX} \quad \ldots\ldots (4.4)$$

Figure 38 shows the pressure profiles of PSS and SS flow scenarios. The pressure at the outer edges is zero and at the inter-cell face is p_F. A quadratic trend of pressure is seen in PSS while a linear trend is seen in SS flow. We will obtain the quadratic expression for pressure in PSS using the Darcy velocity, u given by **Eq. 4.5**.

$$u = -\frac{k}{\mu}\frac{\partial p}{\partial x} \quad \ldots\ldots (4.5)$$

where,

μ, viscosity; cp;

k, permeability; md;

Using **Eq. 4.5** in **Eq. 4.3** and **Eq. 4.4** with specified boundary conditions, we can obtain the expression for pressure in each cell with PSS flow given by **Eq. 4.6** and **Eq. 4.7**.

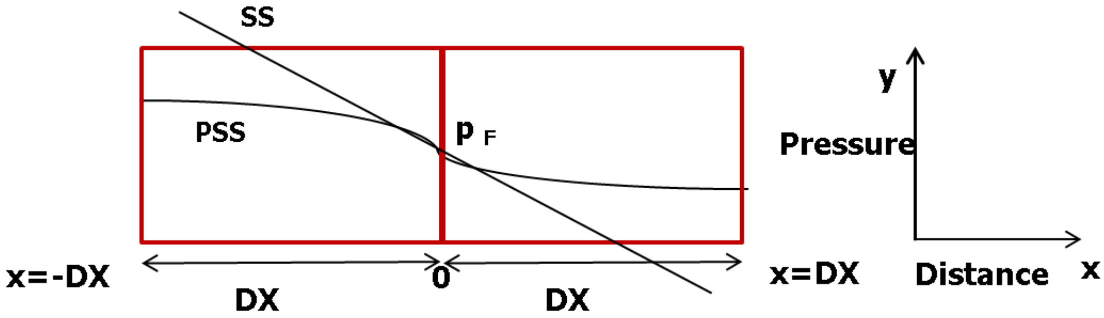

Figure 38: Pressure profile

$$p_l = p_F - \frac{\mu q_F DX}{2kA}\left(\left(\frac{DX + x}{DX}\right)^2 - 1\right) \ldots\ldots\ldots\ldots\ldots\ldots\ldots\ldots\ldots\ldots\ldots\ldots\ldots\ldots\ldots\ldots\ldots\ldots.\ldots\ldots (4.6)$$

$$p_r = p_F + \frac{\mu q_F DX}{2kA}\left(\left(\frac{DX - x}{DX}\right)^2 - 1\right) \ldots\ldots\ldots\ldots\ldots\ldots\ldots\ldots\ldots\ldots\ldots\ldots\ldots\ldots\ldots\ldots\ldots\ldots.\ldots\ldots (4.7)$$

where,

p_l, pressure of the left cell; psi;

p_r, pressure of the right cell; psi;

p_F, pressure at the inter-cell face; psi;

The above equations show a quadratic relationship of pressure with distance, x. For a Steady State scenario, the average pressure and pressure at the center of the cell are the same because of linear relationship of pressure with distance. The same analogy does not work in PSS flow as pressure at the center of the cell may not be the average pressure. If we consider a distance weighted average of the pressure obtained in **Eq. 4.6** and **Eq. 4.7**, we obtain the following expressions for average pressure in each cell.

$$\overline{p_l} = \frac{1}{DX}\int_{-DX}^{0}(p_F - \frac{\mu q_F DX}{2kA}\left\{\left(\frac{DX+x}{DX}\right)^2 - 1\right\})dx \ldots \ldots (4.8)$$

$$\overline{p_r} = \frac{1}{DX}\int_{0}^{DX}(p_F + \frac{\mu q_F DX}{2kA}\left\{\left(\frac{DX-x}{DX}\right)^2 - 1\right\})dx \ldots \ldots (4.9)$$

or,

$$\overline{p_l} = p_F + \frac{\mu q_F DX}{3kA} \ldots \ldots (4.10)$$

$$\overline{p_r} = p_F - \frac{\mu q_F DX}{3kA} \ldots \ldots (4.11)$$

The transmissibility between the cells is given by **Eq. 4.12**.

$$T = \frac{q_F}{\overline{p_l} - \overline{p_r}} \ldots \ldots (4.12)$$

where,

T, inter-cell transmissibility; ft^3/day/psi;

Using the values of average pressures obtained from **Eq. 4.10** and **Eq. 4.11** in **Eq. 4.12**, we obtain the transmissibility for PSS flow given by **Eq. 4.13**.

$$T_{PSS} = \frac{3}{2}\frac{kA}{\mu DX} \ldots \ldots (4.13)$$

But, the known solution of transmissibility between two homogeneous cells is obtained from SS flow given by **Eq. 4.14**.

$$T_{SS} = \frac{kA}{\mu DX} \quad (4.14)$$

So, we have an extra pre-factor 3/2 from PSS solution due to the ambiguity in spatial averaging of pressure in the cell. We think the reason behind getting accurate results for the field case may be due to the compensation of time thresholding for spatial averaging of pressure. This is because we are using the effective pore volume (**Eq. 2.32**) as the weight for averaging pressure in the coarse cell and the effective pore volume contains the time varying exponential term ($e^{-\frac{\tau^2}{4t}}$).

One way to get back the known SS solution in the above case is to remove the quadratic trend in pressure so that pressure varies linearly in the coarse cell. We have tried to apply the same concept in the field case to see the variation of pressure with diffusive time of flight (τ) as τ is considered equivalent of distance in a heterogeneous system.

Figure 39 shows the pressure profile for a local 2x2xN PSS upscaling calculation for the field case. The top left quadrant represents the pressure of the left coarse cell and the bottom right quadrant shows the pressure of the right coarse cell in the upscaling calculation. Both the coarse cell pressures have shown to follow a quadratic trend. The SS pressures are plotted by removing the quadratic trend from the PSS pressures. It is still an open question on how to average pressure in the PSS flow scenario.

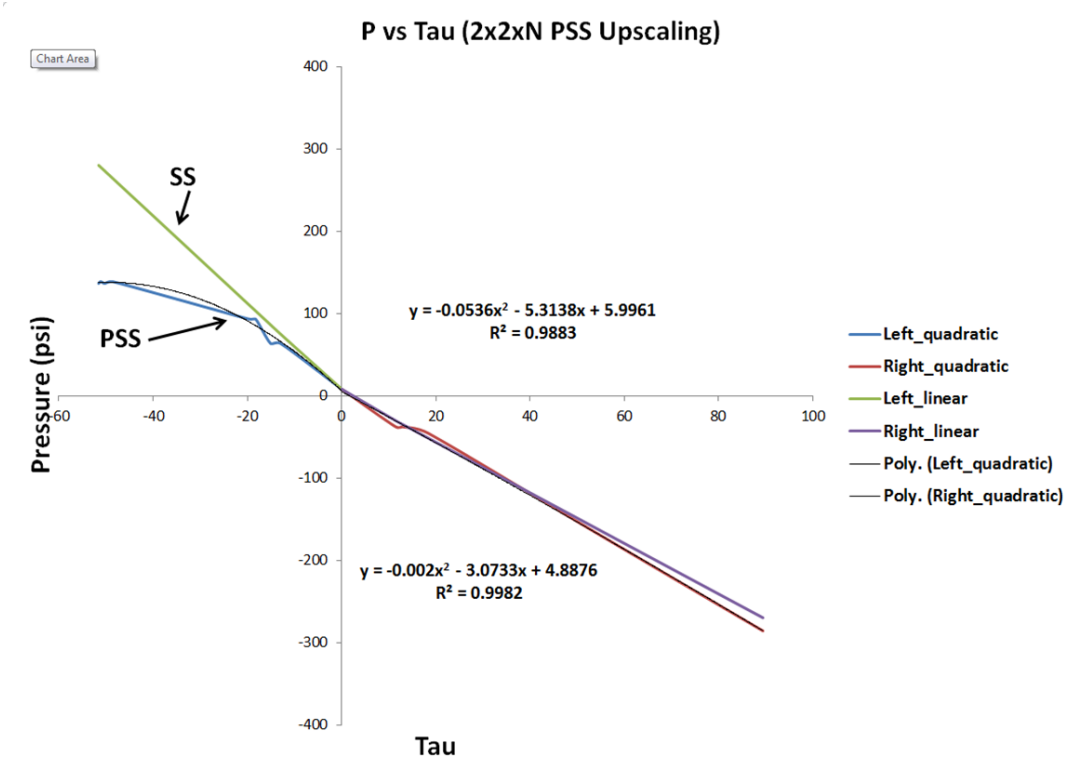

Figure 39: Pressure profile in a local 2x2xN PSS upscaling

CHAPTER V

SUMMARY AND CONCLUSIONS

We developed a novel and accurate local transient flow based upscaling approach. The existing upscaling literature utilizes steady state solutions which may not be applicable to tight (low) permeability unconventional systems, we introduced a transient based upscaling approach to better capture flow dynamics in unconventional reservoirs. The drainage volume concept allows its applicability to unconventional reservoirs although it can also be used in conventional reservoirs. We also have resolved known issues with previously proposed pseudo steady state diffuse source algorithm to account for disconnected volumes in the calculation.

We have successfully applied the pressure transient concepts to calculate the effective coarse cell transmissibilities, on a tight gas reservoir with around 4 million cells. The results demonstrated that we have been able to reduce the simulation time by two orders of magnitude without significant loss of accuracy in performance prediction.

The proposed approach is very general and since, we are using the concept of drainage volume to calculate the transmissibility, we are not constrained to Cartesian shapes for either fine or coarse cells. It is expected that the approach can be applied to completely unstructured problems as there is no specific dependence on the cell geometry in the upscaling calculation.

5.1 Recommendations for future work

Although, the results of diffuse source upscaling on the tight gas reservoir are encouraging, there is scope for additional work. Following are some of the areas identified:

1. The procedure where we set the drainage volume threshold to estimate the time is not general and would benefit from additional investigation.
2. Modified spatial averaging for the coarse cell pressure may remove the incorrect pre-factor and allow better consistency with the steady state results for the long time.
3. The upscaling approach can be tested in conventional reservoirs to explore its applicability.
4. A new upgridding approach can be designed to coarsen adaptively in the areal direction, taking advantage of the unstructured nature of the upscaling approach.
5. Extensions also exist for upscaling of multi-point flux calculations.

REFERENCES

Ambegaokar, V., Halperin, B.I., and Langer, J.S. 1971. Hopping Conductivity in Disordered Systems. *Physical Review B* **4** (8): 2612-2620.

Arbogast, T. and Bryant, S.L. 2002. A Two-Scale Numerical Subgrid Technique for Waterflood Simulations. Society of Petroleum Engineers. DOI: 10.2118/81909-PA.

Barker, J.W. and Thibeau, S. 1997. A Critical Review of the Use of Pseudorelative Permeabilities for Upscaling. Society of Petroleum Engineers. DOI: 10.2118/35491-PA.

Begg, S.H., Carter, R.R., and Dranfield, P. 1989. Assigning Effective Values to Simulator Gridblock Parameters for Heterogeneous Reservoirs. Society of Petroleum Engineers. DOI: 10.2118/16754-PA.

Chen, Y., Durlofsky, L.J., Gerritsen, M. et al. 2003. A Coupled Local–Global Upscaling Approach for Simulating Flow in Highly Heterogeneous Formations. *Advances in Water Resources* **26** (10): 1041-1060. DOI: http://dx.doi.org/10.1016/S0309-1708(03)00101-5

Chen, Z. and Hou, T. 2003. A Mixed Multiscale Finite Element Method for Elliptic Problems with Oscillating Coefficients. *Mathematics of Computation* **72** (242): 541-576.

Darman, N.H., Pickup, G.E., and Sorbie, K.S. 2002. A Comparison of Two-Phase Dynamic Upscaling Methods Based on Fluid Potentials. *Computational Geosciences* **6** (1): 5-27.

Datta-Gupta, A. 2013. Fast Marching Method: A New Paradigm for Modeling Unconventional Reservoirs. College station, Texas: Texas A&M University.

Datta-Gupta, A. and King, M.J. 2007. *Streamline Simulation: Theory and Practice*: Richardson, TX: Society of Petroleum Engineers. Original edition. ISBN 1555631118.

Dijkstra, E.W. 1959. A Note on Two Problems in Connexion with Graphs. *Numerische Mathematik* **1**: 269--271.

Du, S. 2012. Multiscale Reservoir Simulation: Layer Design, Full Field Pseudoization and near Well Modeling, Doctoral dissertation, Texas A&M University. Available electronically from http://hdl. handle. net/1969. 1/148248.

Durlofsky, L.J. 1991. Numerical Calculation of Equivalent Grid Block Permeability Tensors for Heterogeneous Porous Media. *Water Resources Research* **27** (5): 699-708. DOI: 10.1029/91wr00107

Durlofsky, L.J. 2005. Upscaling and Gridding of Fine Scale Geological Models for Flow Simulation. In *8th International Forum on Reservoir Simulation Iles Borromees, Stresa, Italy*:20-24.

Durlofsky, L.J., Milliken, W.J., and Bernath, A. 2000. Scaleup in the near-Well Region. Society of Petroleum Engineers. DOI: 10.2118/61855-PA.

Efendiev, Y.R. and Durlofsky, L.J. 2003. Accurate Subgrid Models for Two-Phase Flow in Heterogeneous Reservoirs. Society of Petroleum Engineers. DOI: 10.2118/79680-ms.

Farmer, C.L. 2002. Upscaling: A Review. *International Journal for Numerical Methods in Fluids* **40** (1-2): 63-78. DOI: 10.1002/fld.267

Gerritsen, M.G. and Durlofsky, L.J. 2005. Modeling Fluid Flow in Oil Reservoirs. *Annu. Rev. Fluid Mech.* **37**: 211-238.

Gomez-Hernandez, J.J. and Journel, A.G. 1994. Stochastic Characterization of Gridblock Permeabilities. Society of Petroleum Engineers. DOI: 10.2118/22187-PA.

Hales, H.B. 1983. Parameterization of Match-Derived Pseudo-Relative Permeabilities. Society of Petroleum Engineers. DOI: 10.2118/11494-MS.

Holden, L. and Nielsen, B.F. 2000. Global Upscaling of Permeability in Heterogeneous Reservoirs; the Output Least Squares (Ols) Method. *Transport in Porous Media* **40** (2): 115-143. DOI: 10.1023/a:1006657515753

Hosseini, S.A. and Kelkar, M. 2010. Analytical Upgridding Method to Preserve Dynamic Flow Behavior. DOI: 10.2118/116113-pa

Hou, T.Y. and Wu, X.-H. 1997. A Multiscale Finite Element Method for Elliptic Problems in Composite Materials and Porous Media. *Journal of Computational Physics* **134** (1): 169-189. DOI: http://dx.doi.org/10.1006/jcph.1997.5682

Jenny, P., Lee, S.H., and Tchelepi, H.A. 2003. Multi-Scale Finite-Volume Method for Elliptic Problems in Subsurface Flow Simulation. *Journal of Computational Physics* **187** (1): 47-67. DOI: http://dx.doi.org/10.1016/S0021-9991(03)00075-5

Kelkar, M. and Perez, G. 2002. *Applied Geostatistics for Reservoir Characterization*: Richardson, Tex.: Society of Petroleum Engineers. Original edition. ISBN 1555630952.

King, M.J. 2007. Upgridding and Upscaling: Current Trends and Future Directions. Society of Petroleum Engineers.

King, M.J. 2011. Upscaling of Geologic Models for Flow Simulation. College station, Texas: Texas A&M University.

King, M.J., Burn, K.S., Wang, P. et al. 2006. Optimal Coarsening of 3d Reservoir Models for Flow Simulation. Society of Petroleum Engineers. DOI: 10.2118/95759-PA.

King, M.J., MacDonald, D.G., Todd, S.P. et al. 1998. Application of Novel Upscaling Approaches to the Magnus and Andrew Reservoirs. Society of Petroleum Engineers. DOI: 10.2118/50643-MS

King, M.J. and Mansfield, M. 1997. Flow Simulation of Geologic Models. Society of Petroleum Engineers. DOI: 10.2118/38877-MS.

King, P.R. 1989. The Use of Renormalization for Calculating Effective Permeability. *Transport in Porous Media* **4** (1): 37-58. DOI: 10.1007/bf00134741

Kulkarni, K.N., Datta-Gupta, A., and Vasco, D.W. 2000. A Streamline Approach for Integrating Transient Pressure Data into High Resolution Reservoir Models. Society of Petroleum Engineers. DOI: 10.2118/65120-ms.

Lee, J. 1982. *Well Testing*: New York: Society of Petroleum Engineers. Original edition. ISBN 0895203170.

Pickup, G.E. and Sorbie, K.S. 1996. The Scaleup of Two-Phase Flow in Porous Media Using Phase Permeability Tensors. DOI: 10.2118/28586-PA.

Renard, P. and de Marsily, G. 1997. Calculating Equivalent Permeability: A Review. *Advances in Water Resources* **20** (5–6): 253-278. DOI: http://dx.doi.org/10.1016/S0309-1708(96)00050-4

RMS, R. 2012. *RMS user guide*: Roxar Software Solutions, 4065 Stavanger, Norway: Roxar ®.

Romeu, R.K. and Noetinger, B. 1995. Calculation of Internodal Transmissivities in Finite Difference Models of Flow in Heterogeneous Porous Media. *Water Resources Research* **31** (4): 943-959. DOI: 10.1029/94wr02422

Sethian, J.A. 1999. Fast Marching Methods. *SIAM REVIEW* **41** (2): 199-235.

Tan, T.B. 1995. Estimating Two and Three Dimensional Pseudo-Relative Permeabilities with Non-Linear Regression. Society of Petroleum Engineers. DOI: 10.2118/29129-MS.

Vasco, D.W., Keers, H., and Karasaki, K. 2000. Estimation of Reservoir Properties Using Transient Pressure Data: An Asymptotic Approach. *Water Resources Research* **36** (12): 3447-3465. DOI: 10.1029/2000wr900179

Warren, J.E. and Price, H.S. 1961. Flow in Heterogeneous Porous Media. Society of Petroleum Engineers. DOI: 10.2118/1579-G.

Wen, X.-H. and Gómez-Hernández, J.J. 1996. Upscaling Hydraulic Conductivities in Heterogeneous Media: An Overview. *Journal of Hydrology* **183** (1–2): ix-xxxii. DOI: http://dx.doi.org/10.1016/S0022-1694(96)80030-8

Wen, X.H., Durlofsky, L.J., and Chen, Y. 2005. Efficient Three-Dimensional Implementation of Local-Global Upscaling for Reservoir Simulation. Society of Petroleum Engineers. DOI: 10.2118/92965-MS.

Xie, J., Gupta, N., King, M.J. et al. 2012. Depth of Investigation and Depletion Behavior in Unconventional Reservoirs Using Fast Marching Methods. Society of Petroleum Engineers. DOI: 10.2118/154532-ms.

Zhou, Y. 2013. Improved Upscaling & Well Placement Strategies for Tight Gas Reservoir Simulation and Management, Doctoral dissertation, Texas A & M University. Available electronically from http://hdl. handle. net/1969. 1/151291.

Zhou, Y. and King, M.J. 2011. Improved Upscaling for Flow Simulation of Tight Gas Reservoir Models. DOI: 10.2118/147355-MS.

APPENDIX A

DIJKSTRA'S METHOD

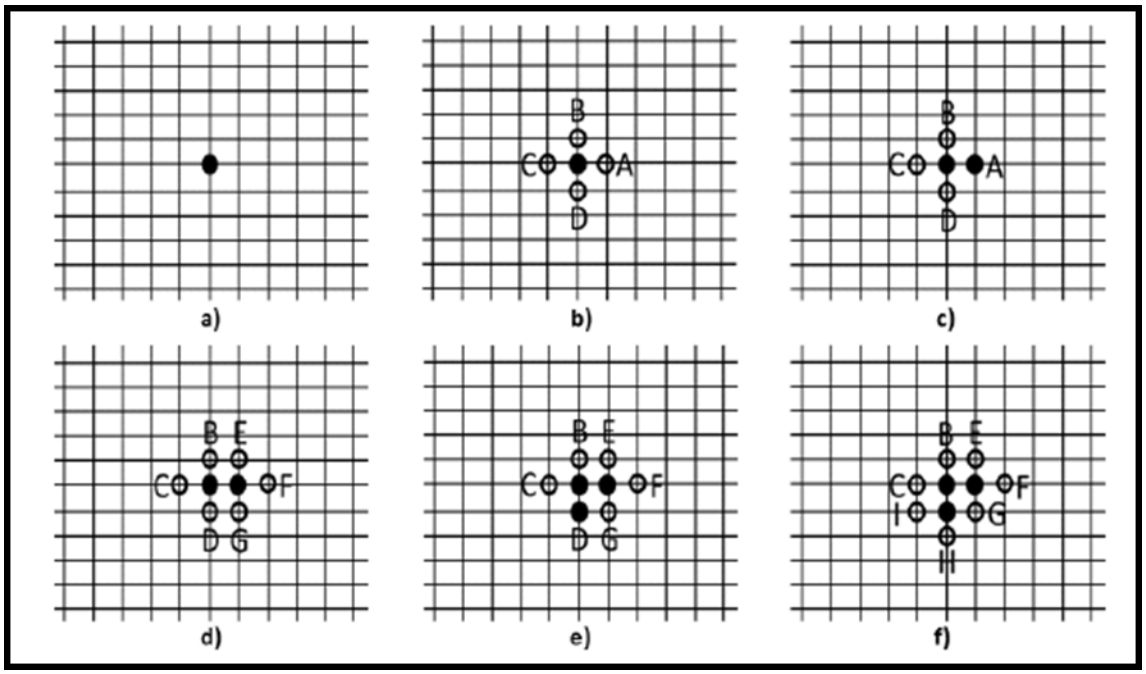

Figure 40: Dijkstra's method (Xie et al. 2012)

Following steps explain the solution of Eikonal equation using Dijkstra (1959) method from top left to bottom right as shown in **Figure 40**.

1. Label the well location(producer/injector) as an accepted node with $\tau = 0$
2. Mark all neighboring nodes A, B, C, D and calculate the diffusive time of flight to all the neighboring nodes
3. Accept the node with minimum τ value and include the new neighboring nodes for accepted node consideration with minimum τ.
4. Repeat steps 2 to 4 until all the nodes in the mesh are accepted.

APPENDIX B

EXPRESSION FOR DRAINAGE VOLUME

Improved geometric pressure approximation formulation is given by

$$c_t \frac{\partial p}{\partial t} = \frac{\partial q}{\partial V_p(\tau)} \cong -\frac{q_w}{V_p(t)} e^{-\frac{\tau^2}{4t}} \dots\dots\dots\dots\dots\dots\dots\dots\dots\dots\dots\dots\dots\dots\dots\dots\dots\dots\dots\dots\dots\dots\dots (B.1)$$

Integrating the above equation from a finite volume of $V_p(t)$ to infinity where q=0, we get

$$q(\tau, t) = \frac{q_w}{V_p(t)} \int_{V_p(\tau)}^{\infty} dV_p(\tau) e^{-\frac{\tau^2}{4t}} \dots\dots\dots\dots\dots\dots\dots\dots\dots\dots\dots\dots\dots\dots\dots\dots\dots\dots\dots\dots . (B.2)$$

The boundary condition at the wellbore ($V_p(\tau) = 0; q = q_w$) now provides the equation for $V_p(t)$.

$$V_p(t) = \int_0^{\infty} dV_p(\tau) e^{-\frac{\tau^2}{4t}} \dots\dots\dots\dots\dots\dots\dots\dots\dots\dots\dots\dots\dots\dots\dots\dots\dots\dots\dots\dots\dots\dots\dots\dots . (B.3)$$

$dV_p(\tau)$ can be written in terms of the Dirac delta function as

$$dV_p(\tau) \cong \sum_j PV_m \delta(\tau - \tau_m) d\tau \dots\dots\dots\dots\dots\dots\dots\dots\dots\dots\dots\dots\dots\dots\dots\dots\dots\dots\dots\dots\dots .. (B.4)$$

Substituting **Eq. (B.4)** in **Eq. (B.3)**, we have

$$V_p(t) \cong \sum_j PV_m \int_o^{\infty} \delta(\tau - \tau_m) e^{-\frac{\tau^2}{4t}} d\tau \dots\dots\dots\dots\dots\dots\dots\dots\dots\dots\dots\dots\dots\dots\dots\dots\dots\dots\dots (B.5)$$

The integral of a Dirac delta function becomes the integrand itself. Therefore, we have the final expression for $V_p(t)$ given by

$$V_p(t) \cong \sum_j PV_j e^{-\frac{\tau_j^2}{4t}} \dots\dots\dots\dots\dots\dots\dots\dots\dots\dots\dots\dots\dots\dots\dots\dots\dots\dots\dots\dots\dots\dots\dots\dots\dots\dots\dots\dots (B.6)$$